remote sensing

MDPI

Article

Seasonal Variations in the Rainfall Kinetic Energy Estimation and the Dual-Polarization Radar Quantitative Precipitation Estimation Under Different Rainfall Types in the Tianshan Mountains, China

Yong Zeng [1,2,3,4,*], Lianmei Yang [1,2,3,4], Zepeng Tong [1,2,3,4], Yufei Jiang [1,2,3,4], Abuduwaili Abulikemu [5], Xinyu Lu [1,2,3,4] and Xiaomeng Li [1,2,3,4]

1 Institute of Desert Meteorology, China Meteorological Administration, Urumqi 830002, China; yanglm@idm.cn (L.Y.); tongzp@idm.cn (Z.T.); jiangyf@idm.cn (Y.J.); luxy@idm.cn (X.L.); lixm@idm.cn (X.L.)
2 Xinjiang Innovation Institute of Cloud Water Resource Development and Utilization, Urumqi 830002, China
3 Xinjiang Cloud Precipitation Physics and Cloud Water Resources Development Laboratory, Urumqi 830002, China
4 Field Scientific Observation Base of Cloud Precipitation Physics in West Tianshan Mountains, Xinyuan 844900, China
5 Xinjiang Key Laboratory of Oasis Ecology, College of Geography and Remote Sensing Sciences, Xinjiang University, Urumqi 830017, China; abduwaly@xju.edu.cn
* Correspondence: zengyong@idm.cn; Tel.: +86-150-9961-0397

Abstract: Raindrop size distribution (DSD) has an essential effect on rainfall kinetic energy estimation (RKEE) and dual-polarization radar quantitative precipitation estimation (QPE); DSD is a key factor for establishing a dual-polarization radar QPE scheme and RKEE scheme, particularly in mountainous areas. To improve the understanding of seasonal DSD-based RKEE, dual-polarization radar QPE, and the impact of rainfall types and classification methods, we investigated RKEE schemes and dual-polarimetric radar QPE algorithms across seasons and rainfall types based on two classic classification methods (BR09 and BR03) and DSD data from a disdrometer in the Tianshan Mountains during 2020–2022. Two RKEE schemes were established: the rainfall kinetic energy flux–rain rate (KE_{time}–R) and the rainfall kinetic energy content–mass-weighted mean diameter (KE_{mm}–D_m). Both showed seasonal variation, whether it was stratiform rainfall or convective rainfall, under BR03 and BR09. Both schemes had excellent performance, especially the KE_{mm}–D_m relationship across seasons and rainfall types. In addition, four QPE schemes for dual-polarimetric radar—$R(K_{dp})$, $R(Z_h)$, $R(K_{dp},Z_{dr})$, and $R(Z_h,Z_{dr})$—were established, and exhibited characteristics that varied with season and rainfall type. Overall, the performance of the single-parameter algorithms was inferior to that of the double-parameter algorithms, and the performance of the $R(Z_h)$ algorithm was inferior to that of the $R(K_{dp})$ algorithm. The results of this study show that it is necessary to consider different rainfall types and seasons, as well as classification methods of rainfall types, when applying RKEE and dual-polarization radar QPE. In this process, choosing a suitable estimator—$KE_{time}(R)$, $KE_{mm}(D_m)$, $R(K_{dp})$, $R(Z_h)$, $R(K_{dp},Z_{dr})$, or $R(Z_h,Z_{dr})$—is key to improving the accuracy of estimating the rainfall KE and R.

Keywords: seasonal variation; rainfall kinetic energy estimation; dual-polarization radar quantitative precipitation estimation; rainfall type; Tianshan mountains

check for updates

Citation: Zeng, Y.; Yang, L.; Tong, Z.; Jiang, Y.; Abulikemu, A.; Lu, X.; Li, X. Seasonal Variations in the Rainfall Kinetic Energy Estimation and the Dual-Polarization Radar Quantitative Precipitation Estimation Under Different Rainfall Types in the Tianshan Mountains, China. *Remote Sens.* **2024**, *16*, 3859. https://doi.org/10.3390/rs16203859

Academic Editor: Gyuwon Lee

Received: 12 September 2024
Revised: 9 October 2024
Accepted: 15 October 2024
Published: 17 October 2024

Copyright: © 2024 by the authors. Licensee MDPI, Basel, Switzerland. This article is an open access article distributed under the terms and conditions of the Creative Commons Attribution (CC BY) license (https://creativecommons.org/licenses/by/4.0/).

1. Introduction

Raindrop size distribution (DSD) is important and fundamental for enriching our knowledge of the microphysical characteristics and processes of rainfall [1–3]. Moreover, DSD plays a key role in rainfall kinetic energy estimation (RKEE), which can significantly

improve its accuracy [4–9]. More importantly, DSD has significant implications for enhancing the quantitative precipitation estimation (QPE) capabilities of both space-borne and ground-based radars [10–15].

DSD exhibits diverse characteristics worldwide owing to the influence of many factors, including the climate region, geographical location, terrain, season, rainfall type, and the weather system [16–23]. Researchers have conducted in-depth studies on DSD in many regions of China, revealing that the particularities of DSD in southern China, northern China, eastern China, and the Qinghai–Tibet Plateau are directly affected by monsoons [24–34]. The diversity of DSD directly leads to differences in the RKEE schemes derived from DSD in different climatic regions, geographical locations, terrains, seasons, rainfall types, and weather systems [9,28,35,36]. Seela et al. [9] established RKEE schemes for 14 tropical cyclones observed in Palau. Wen et al. [28] analyzed the seasonal variation in RKEE schemes in eastern China and concluded that the variability of DSD is an important reason for the diversity of RKEE schemes. Janapati [35] analyzed in detail and provided RKEE schemes for three locations in northern Taiwan during different seasons and concluded that the diversity of RKEE is caused by the variation in DSD with the location and season. Wu et al. [36] constructed RKEE schemes in southwestern China and showed that the diversity in RKEEs among different rainfall types was caused by DSD variation. In summary, various conditions that determine the diversity of DSD cause RKEE schemes to exhibit diverse characteristics. Therefore, it is necessary to construct separate RKEE schemes for different seasons and rainfall types in certain regions.

Similarly, the diversity of DSD directly leads to differences in QPE algorithms derived from DSD in different climate regions, geographical locations, terrains, seasons, rainfall types, and weather systems [20–27]. QPE algorithms for single-polarization radars have been structured in many countries based on rain rates (R) and radar reflectivity factors derived from DSD [37–44]. However, an increasing number of studies have indicated that the performance of QPE algorithms for single-polarization radars is worse than that for dual-polarization radars [13–15,45–49]. Zhang et al. [13] established three QPE algorithms for dual-polarization radars in Beijing based on DSD data and emphasized that the QPE estimator containing R, the specific differential phase (K_{dp}), and differential reflectivity (Z_{dr}) [i.e., $R(K_{dp},Z_{dr})$] performs the best. Chen et al. [14] constructed QPE algorithms for dual-polarization radars in eastern China and emphasized that the QPE algorithms exhibit variability in different convective weather systems. Li et al. [48] established four QPE algorithms for dual-polarization radars over the northeastern Qinghai–Tibet Plateau and concluded that double-parameter QPE algorithms were superior to single-parameter QPE algorithms. You et al. [49] analyzed QPE algorithms in the Halla Mountains on Jeju Island, South Korea, based on DSD data from 10 particle size velocity (PARSIVEL) disdrometers, and concluded that terrain plays an important role in the diversity of QPE algorithms. In short, many factors that affect the characteristics of DSD, including climate region, geographical location, terrain, season, rainfall type, and weather system, also affect dual-polarization radars QPE algorithms. Therefore, the establishment of dual-polarization radar QPE algorithms for various rainfall types and seasons is of great value in certain regions.

Xinjiang is located in the northwest of China and is a typical arid region [50]. Due to the strong influence of terrain uplift, the Tianshan Mountains have become the precipitation center of Xinjiang [51,52]. Some studies have partially clarified the specificity of DSD [53,54] and developed RKEE schemes [55–57] and QPE algorithms [55–61] using DSD information from the Tianshan Mountains. Zeng et al. [54] investigated the features of DSD during the rainy season (April to October) and emphasized that DSD in the Tianshan Mountains has unique characteristics compared with that in other regions. Zeng et al. [55] constructed RKEE schemes for overall rainfall in each season over the Tianshan Mountains and established RKEE schemes for different types of rainfall in summer [56]. In addition, QPE algorithms for single-polarization radars were established in the Tianshan Mountains, demonstrating significant differences compared with those in other regions [58]. Further-

more, Zeng et al. [60] constructed dual-polarization radar QPE algorithms for the summer over the Tianshan Mountains and suggested that dual-polarization radar had significantly better QPE performance compared with single-polarization radar. However, the RKEE schemes and dual-polarization radar QPE algorithms for different rainfall types in this area under the two classic rainfall classification methods proposed by Bringi [18] and Bringi [62] remain unknown, and their differences in different seasons have not been studied.

To reveal DSD-based RKEE schemes and dual-polarization radar QPE algorithms under different rainfall types and to explore the effects of the seasons on RKEE schemes and dual-polarization radar QPE algorithms in the Tianshan Mountains, a study based on the DSD collected from the Tianshan Mountains during 2020–2022 was conducted.

2. Data and Methodology

2.1. Study Area and Dataset

The Tianshan Mountains are located in the north of the Qinghai–Tibet Plateau, with the main body located in central Xinjiang, China (Figure 1a). Within this region, Zhaosu (1851 m a.s.l.; 43.14°N, 81.13°E) was the focus area for this study (Figure 1b); the DSD dataset for Zhaosu from 2020 to 2022 was collected based on a second-generation OTT Particle Size Velocity (PARSIVEL^2) disdrometer manufactured by OTT Hydromet (Kempten, Germany) [59]. The observation area of Zeng et al. [55] was Xinyuan (928 m a.s.l.; 43.45°N, 83.25°E); they also used a PARSIVEL^2 disdrometer, and its location is also displayed in Figure 1b. DSD information was obtained by simultaneously recording the particle sizes and fall speeds within a resolution of 1 min [63,64]. More and more studies have used PARSIVEL^2 disdrometers to conduct research on DSD because of their excellent performance [9,43,44,49,53–60,65–68]. However, as the high altitude of Zhaosu results in no rainfall in this region during winter [59], this study only considered data from the spring, summer, and fall.

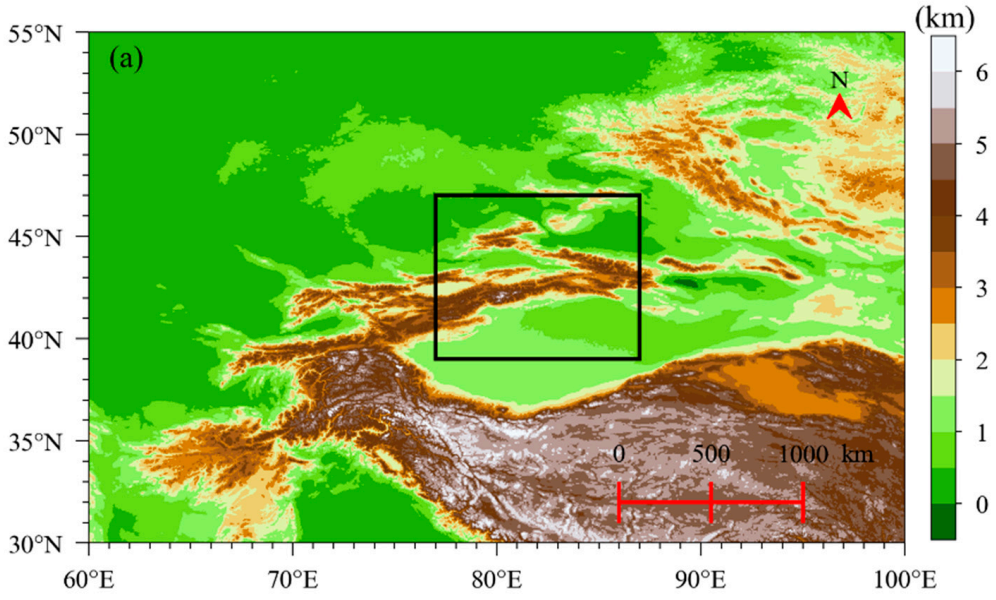

Figure 1. *Cont.*

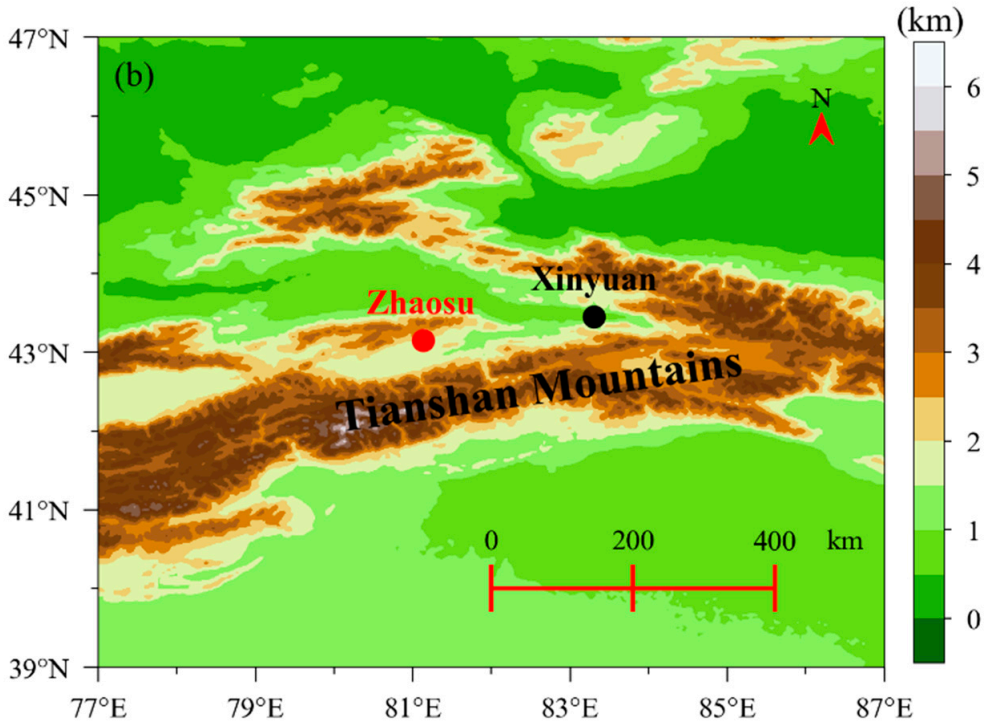

Figure 1. (**a**) Topography (m) and location of the Tianshan Mountains, and (**b**) locations of Zhaosu (red dot) and Xinyuan (black dot; Zeng et al. [55]).

2.2. Quality Control of DSD Data

The quality of the DSD data is affected by many factors, so the quality control processing of the DSD data is crucial. The most critical influencing factors that cannot be ignored are as follows: low signal-to-noise ratio [12,69], low rain rate or number of raindrops during the sampling time [70], and splashing effects or strong winds [64,71]. Therefore, eliminating the impact of these three aspects is important to obtain more accurate DSD data. Previous studies of DSD over the Tianshan Mountains have implemented strict quality control [55–59]. After data quality control, 15,318, 20,785, and 5151 DSD samples were used in the Tianshan Mountains from the spring to fall in Zhaosu, respectively [59].

2.3. RKEE

Rainfall kinetic energy is usually expressed as KE_{time} (i.e., rainfall kinetic energy flux, J m^{-2} h^{-1}) and KE_{mm} (i.e., rainfall kinetic energy content, J m^{-2} mm^{-1}) [4,9,35,36,72,73], which can be calculated using Equations (1) and (2), respectively:

$$KE_{time} = \left(\frac{\pi}{12}\right) \times \left(\frac{1}{10^6}\right) \times \left(\frac{3600}{\Delta t}\right) \times \left(\frac{1}{A_{eff}(D_i)}\right) \sum_{i=1}^{32} n_i \times {D_i}^3 \times (V(D_i))^2 \quad (1)$$

$$KE_{mm} = \frac{KE_{time}}{R} \quad (2)$$

where Δt (s) is the sampling time (60 s); D_i (mm) represents the raindrop diameter; $V(D_i)$ [m s^{-1}] is the raindrop velocity; and A_{eff} (D_i) [m^2] and R (mm h^{-1}) are the effective sampling area [63,74,75] and rain rate, respectively, which can be calculated using Equations (3) and (4):

$$A_{eff}(D_i) = 10^{-6} \times 180 \times \left(30 - \frac{D_i}{2}\right) \quad (3)$$

$$R = \frac{6\pi}{10^4} \times \sum_{i=1}^{32} N(D_i) \times {D_i}^3 \times V(D_i) \times \Delta D_i \quad (4)$$

where ΔD_i (mm) represents the diameter interval and $N(D_i)$ [m^{-3} mm^{-1}] represents DSD, which can be calculated using Equation (5):

$$N(D_i) = \sum_{j=1}^{32} \frac{n_{ij}}{A_{eff}(D_i) \times \Delta t \times V(D_i) \times \Delta D_i} \quad (5)$$

where n_{ij} is the number of drops.

The DSD-based RKEE schemes, including $KE_{time}(R)$ and $KE_{mm}(D_m)$ [5–7,9,35,55–57], are as follows:

$$KE_{time}(R) = a \times R^b \quad (6)$$

$$KE_{mm}(D_m) = c \times D_m^2 + d \times D_m + e \quad (7)$$

where a, b, c, d, and e are the corresponding coefficients of the RKEE schemes and D_m (mm) is the mass-weighted mean diameter [76], as follows:

$$D_m = \frac{\sum_{i=1}^{32} N(D_i) \times D_i^4 \times \Delta D_i}{\sum_{i=1}^{32} N(D_i) \times D_i^3 \times \Delta D_i} \quad (8)$$

2.4. QPE for Dual-Polarization Radar

The DSD-based dual-polarization radar QPE algorithms are particularly valuable in enhancing the QPE capability [13,26,27,29–31,56,60]. These algorithms are constructed using the variables of the dual-polarization radar, including (1) $Z_{h/v}$ (i.e., radar reflectivity at horizontal or vertical polarization, mm^6 m^{-3}), (2) Z_{dr} (i.e., differential reflectivity, dB), and (3) K_{dp} (i.e., specific differential phase, $^\circ$ km^{-1}), which can be derived based on the T-matrix scattering method [47,77–79] as follows:

$$Z_{h/v} = \left(\frac{4 \times \lambda^4}{\pi^4 \times |K_w|^2} \right) \times \int_{D_{min}}^{D_{max}} |f_{hh/vv}(D)|^2 \times N(D) \times dD \quad (9)$$

$$Z_{dr} = 10 \times \log_{10} \left(\frac{Z_h}{Z_v} \right) \quad (10)$$

$$K_{dp} = 10^{-3} \times \frac{180}{\pi} \times \lambda \times Re \left\{ \int_{Dmin}^{D_{max}} [f_h(D) - f_v(D)] \times N(D) \times dD \right\} \quad (11)$$

where D_{max} is 8 mm, according to the DSD data in this study; K_w (−) and λ (mm) are the dielectric constant of water (0.9639) and the dual-polarization radar wavelength (33.3 mm for the X-band in this study), respectively; and $f_{h/v}(D)$ and $f_{hh/vv}(D)$ represent the forward scattering and backscattering amplitudes of a raindrop, respectively. In this study, the axis–ratio relation reported by Brandes [47] constrained the raindrops.

The DSD-based dual-polarization radar QPE algorithms, including (1) $R(Z_h)$, (2) $R(K_{dp})$, (3) $R(Z_h,Z_{dr})$, and (4) $R(K_{dp},Z_{dr})$, are as follows:

$$R(Z_h) = f \times Z_h^g \quad (12)$$

$$R\left(K_{dp}\right) = h \times K_{dp}^i \quad (13)$$

$$R(Z_h, Z_{dr}) = j \times Z_h^k \times 10^{l \times Z_{dr}} \quad (14)$$

$$R\left(K_{dp}, Z_{dr}\right) = m \times K_{dp}^n \times 10^{o \times Z_{dr}} \quad (15)$$

where f, g, h, i, j, k, l, m, n, and o are the coefficients of the corresponding dual-polarization radar QPE algorithms.

2.5. Assessing RKEE Scheme and Dual-Polarization Radar QPE Algorithm Accuracy

The values of KE_{time}, KE_{mm}, and R calculated using Equations (1), (2), and (4) were used to assess the accuracy of the RKEE schemes (Equations (6) and (7)) and the dual-polarization radar QPE algorithms (Equations (12)–(15)). The correlation coefficient (CC), normalized mean absolute error (NMAE), and root mean square error (RMSE) were used to assess the estimators:

$$\mathrm{CC} = \frac{\sum_{i=1}^{n}\left(M_i - \overline{M}\right) \times \left(M_{e,i} - \overline{M_e}\right)}{\sqrt{\sum_{i=1}^{n}\left(M_i - \overline{M}\right)^2} \times \sqrt{\sum_{i=1}^{n}\left(M_{e,i} - \overline{M_e}\right)^2}} \tag{16}$$

$$\mathrm{NMAE} = \frac{\frac{1}{n} \times \sum_{i=1}^{n}\left|M_{e,i} - M_i\right|}{\overline{M}} \tag{17}$$

$$\mathrm{RMSE} = \sqrt{\frac{1}{n} \times \sum_{i=1}^{n}\left(M_{e,i} - M_i\right)^2} \tag{18}$$

where M_i and $\overline{M}$ represent the individual and average KE_{time}, KE_{mm}, and R calculated from the DSD data, respectively; and $M_{e,i}$ and $\overline{M_e}$ are the individual and average KE_{time}, KE_{mm}, and R derived from the RKEE schemes and dual-polarization radar QPE algorithms, respectively.

2.6. Classification of Rainfall Types

Stratiform and convective rainfall are the two basic rainfall types, and many researchers have proposed classification methods for these rainfall types [12,17,18,62,76,80]. Here, we used two classic classification methods of rainfall types to divide DSD data into stratiform and convective rainfall. Specifically, the first classification method was reported by Bringi et al. [62], based on the $\log_{10}N_w$ (normalized intercept parameter)–D_0 (median volume diameter) space (BR09) [36,59,62,81,82]. The second classification scheme was reported by Bringi et al. [18], considering R and the standard deviation of R (BR03) [18–25]. The simultaneous application of these two classification schemes (BR09 and BR03) was based on their widespread recognition and the characteristics of rainfall in arid regions. BR09 and BR03 are both classic classification schemes for rainfall types, which have been applied in many regions, especially the BR03 classification. More importantly, the Tianshan Mountains are located in arid areas with insufficient water vapor supply, and the convective rainfall in this region has the characteristics of a short duration, a high variability, and a relatively low R compared to monsoon areas [50–52]. BR03 can be specifically expressed when there is at least 10 consecutive 1 min rainfall samples; the rainfall is determined to be stratiform rainfall (convective rainfall) if R is >0.5 (5) mm h^{-1} and the standard deviation of R is < (>) 1.5 mm h^{-1}. In previous studies based on the BR03, we found that even in summer, there were fewer convective rainfall samples in the Tianshan Mountains [53,54,56,58], which were affected by the short duration, high variability, and low R of convective rainfall in the region. Based on this, the widely recognized BR09 has also been applied in this study. Specifically, BR09 can be expressed as samples located below (above) the equation $\log_{10}N_w = -1.6D_0 + 6.3$ in the $\log_{10}N_w - D_0$ space that are classified as stratiform rainfall (convective rainfall). It should be noted that we recognize both of these two classic classification methods, and there is no superiority or inferiority between BR09 and BR03; only the classification principles are different. Furthermore, the simultaneous application of BR09 and BR03 provided convenience for comparing different classification schemes of rainfall types in this study and comparing them with previous studies based only on one classification scheme of rainfall type in other regions. After the classification of rainfall types for all DSD samples, the number of DSD samples for stratiform rainfall (convective rainfall) classified by BR09 was 40,380 (871), while the number classified by BR03 was 10,349 (228). In terms of seasons, for stratiform rainfall under BR09 (BR09_S), the numbers of the samples were 15,115, 20,148, and 5117 from spring to fall, respectively, whereas for convective rainfall under BR09 (BR09_C), the numbers of the samples were 202,

636, and 33 from spring to fall, respectively. For stratiform rainfall under BR03 (BR03_S), the numbers of the samples were 4523, 4734, and 1092 from spring to fall, respectively, while for convective rainfall under BR03 (BR03_C), the numbers of the samples were 119 and 109 in spring and summer, respectively. Notably, there were no samples of convective rainfall in the fall under BR03. For a more detailed explanation of the DSD data and the process of classifying rainfall types in this study, please refer to Zeng et al. [59].

3. Results

3.1. Seasonal RKEE Variation

As "the water tower of central Asia", heavy rainfall in the Tianshan Mountains often causes landslides, mudslides, and floods, owing to the steep terrain; the degree of damage caused by these secondary disasters can be estimated to some extent by rainfall kinetic energy (*KE*), including KE_{time} and KE_{mm} [57,83]. Obtaining the rainfall *KE* from DSD information overcomes the limitations of expensive direct measurement instruments and is an important method for obtaining rainfall *KE* [4]. Figure 2 shows seasonal variations in KE_{time} and KE_{mm}. For the entire data and spring, the peak distribution of KE_{time} was 4.5 J m^{-2} h^{-1}; for summer and fall, KE_{time} was mostly distributed around 6.5 and 3.0 J m^{-2} h^{-1}, respectively; mean KE_{time} (purple solid line) was the largest (smallest) at 29.418 (14.006) J m^{-2} h^{-1} in the summer (fall) (Figure 2a). The peak distribution of KE_{mm} for the entire data and the three seasons was 7.6, 6.8, 8.0, and 8.2 J m^{-2} mm^{-1}, respectively, and mean KE_{mm} (purple solid line) was largest (smallest) at 12.307 (9.826) J m^{-2} mm^{-1} in summer (spring) (Figure 2b).

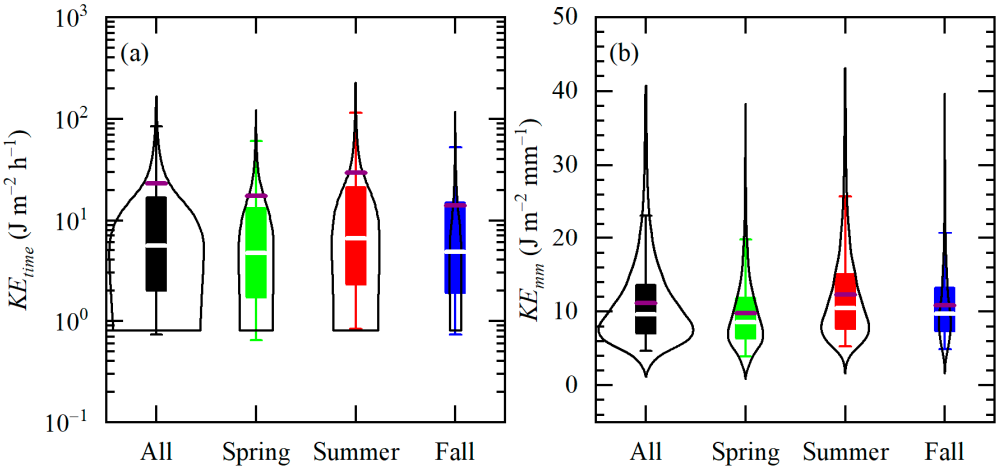

Figure 2. Seasonal variations in the distributions of (**a**) KE_{time} and (**b**) KE_{mm} at Zhaosu.

The scatterplots of KE_{time} vs. R for the entire dataset and the KE_{time}–R relationship across the seasons are shown in Figure 3. For ease of comparison, previous results from Zeng et al. [55], Seela et al. [83], and Wu et al. [36] are also shown. For the entire dataset, the KE_{time}–R relation was $KE_{time} = 12.495R^{1.285}$. The fitting curves for summer and fall were similar to those for the entire dataset. For the same R, KE_{time} was slightly smaller in spring or fall than in summer. Compared with Zeng et al. [55], regardless of the entire dataset or different seasons, given the R value, the KE_{time} of Zhaosu was almost always greater than that of Xinyuan. The KE_{time}–R relationship for the entire data at Enshi (a southwestern mountain area of China), as reported by Wu et al. [36], was higher than that for the entire data at Zhaosu when $R < 35.0$ mm h^{-1}, and vice versa when $R > 35.0$ mm h^{-1}. Compared with all the above results, for the same R, Seela et al. [83] reported the smallest KE_{time} for typhoons in Palau, an island in the Western Pacific. The variation among each curve in Figure 3 was relevant to their own elevation or climate conditions.

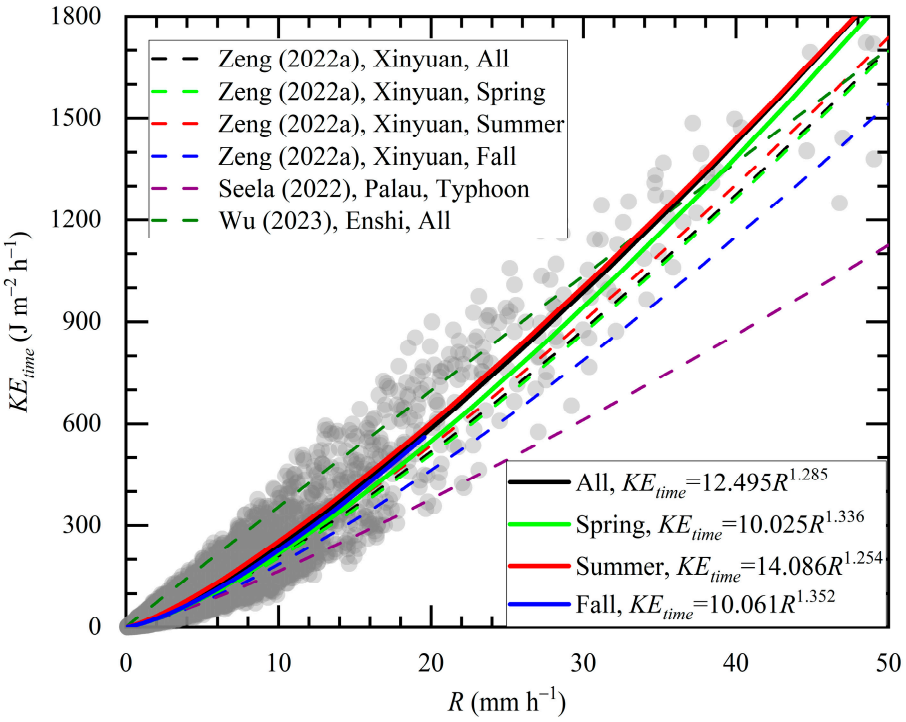

Figure 3. Scatterplots of KE_{time} vs. R for the entire data and the fitted KE_{time}–R relationship across seasons at Zhaosu. Dashed lines represent the KE_{time}–R relationship reported by Zeng et al. [55], Seela et al. [83], and Wu et al. [36].

For RKEE, the KE_{mm}–D_m relationship is also an important RKEE scheme. Figure 4 shows scatterplots of KE_{mm} vs. D_m for the entire dataset and for different seasons at Zhaosu compared with those for previous results [55,83]. For the entire dataset, the KE_{mm}–D_m relationship was $KE_{mm} = -2.260D_m^2 + 21.953D_m - 8.899$. The fitting curves across the seasons were very close to those for the entire dataset until D_m was >3.6 mm. When D_m > 3.2 mm, as D_m increased, the difference between KE_{mm} in summer and that in spring and fall gradually increased. However, the seasonal variation in KE_{mm} was not as significant as that at Xinyuan [55]. Another difference between Zhaosu and Xinyuan was that, for a given D_m value, a larger KE_{mm} was observed in Zhaosu than in Xinyuan, whereas the opposite was true for D_m > 2.8 mm in fall. Compared with all the above results, for 0.6 mm < D_m < 3.8 mm, Seela et al. [83] reported the smallest KE_{mm} of KE_{mm}–D_m relationship for a typhoon in Palau, Western Pacific.

To evaluate the accuracy of the derived RKEE schemes, we compared the estimated rainfall KE for different RKEE schemes, as shown in Figures 3 and 4, with the rainfall KE directly derived from DSD based on Equations (1) and (2). Figure 5 shows scatterplots of KE_{time} and KE_{mm} computed from the derived RKEE schemes and DSD in terms of the CC, RMSE, and NMAE. The performances of the RKEE schemes of KE_{mm} were superior to those of KE_{time} for all seasons and the entire dataset, and were characterized by more clustered scatterers along the 1:1 line and larger CC (>0.99). For the RKEE schemes of KE_{mm} across seasons, the performance of KE_{mm} in summer was superior to that in spring and fall, with a larger CC (0.9965) and smaller RMSE (0.5496 J m^{-2} mm^{-1}) and NMAE (0.0334 J m^{-2} mm^{-1}). Similarly, the performance of KE_{time} in summer was superior to that in spring and fall, with a larger CC (0.9698) and smaller NMAE (0.2636 J m^{-2} h^{-1}), while a larger RMSE in summer was mainly caused by the larger KE_{time}, as shown in Figure 2a. This may be related to the fact that summer has more samples compared to other seasons. Overall, the RKEE schemes performed well for both the entire dataset and the different seasons.

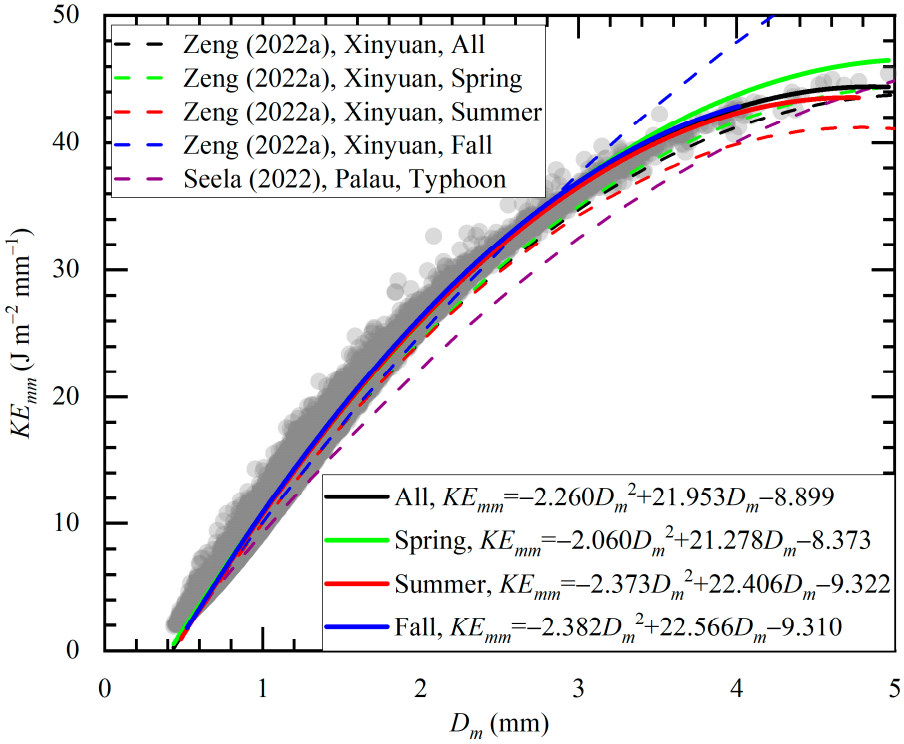

Figure 4. Scatterplots of KE_{mm} vs. D_m for the entire data and the seasonal variation in fitted KE_{mm}–D_m at Zhaosu. Dashed lines represent the KE_{mm}–D_m relationship reported by Zeng et al. [55] and Seela et al. [83].

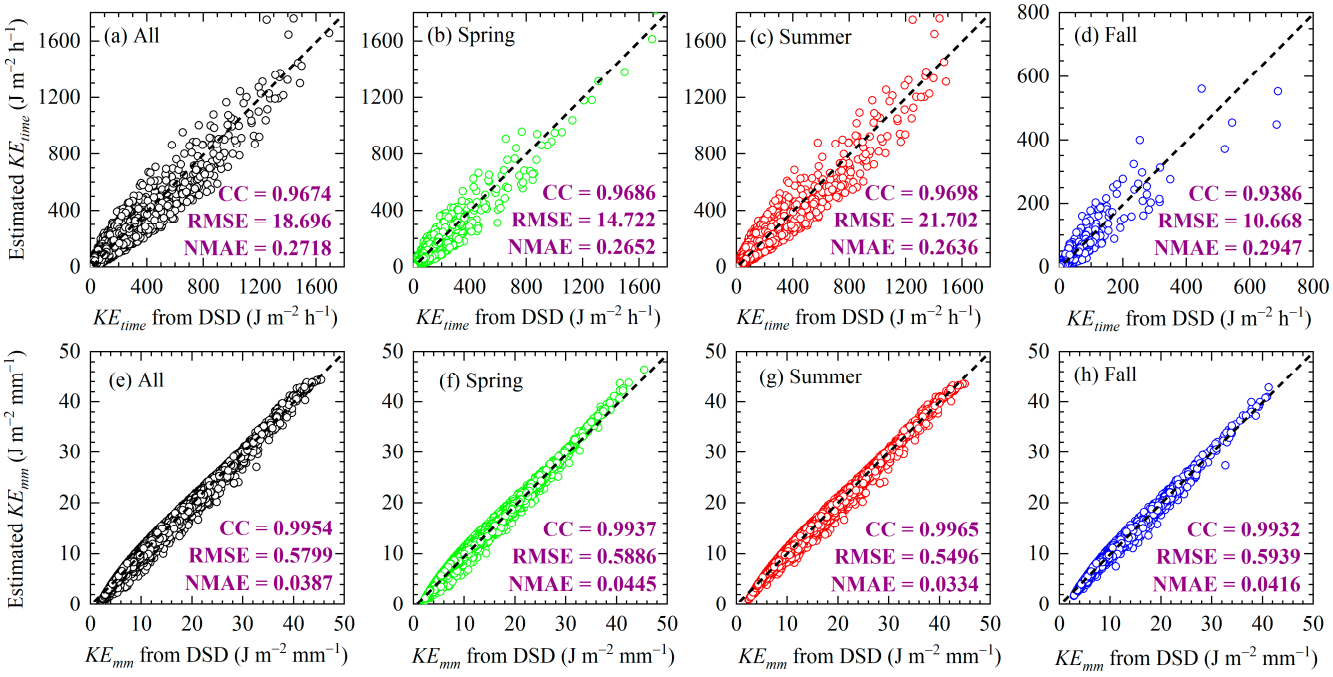

Figure 5. Scatterplot of estimated KE_{time} from RKEE schemes versus KE_{time} calculated from DSD for (**a**) the entire data, (**b**) spring, (**c**) summer, and (**d**) fall at Zhaosu. Scatterplot of estimated KE_{mm} from RKEE schemes versus the KE_{mm} calculated from DSD for (**e**) the entire data, (**f**) spring, (**g**) summer, and (**h**) fall at Zhaosu in Tianshan Mountains. Black dashed lines represent the 1:1 relationship.

3.2. Seasonal RKEE Variation for Different Rainfall Types

Stratiform and convective rainfall are two basic types of rainfall with significant differences in their microphysical characteristics [17–25,62,80–82]. Therefore, it is necessary to explore the RKEE for different rainfall types. Figure 6 shows the seasonal variations in the distributions of KE_{time} and KE_{mm} for stratiform and convective rainfall under BR09 and BR03 at Zhaosu. For stratiform rainfall under BR09 (BR09_S), the peak distribution of KE_{time} was 5.0 J m^{-2} h^{-1}, with a mean KE_{time} (purple solid line) at its largest (smallest) at 17.535 (12.489) J m^{-2} h^{-1} in the summer (spring) (Figure 6a). For convective rainfall under BR09 (BR09_C), the KE_{time} with the highest distribution across the different seasons was ~260.0 J m^{-2} h^{-1}, and the mean KE_{time} was largest (smallest) at 405.907 (249.190) J m^{-2} h^{-1} in summer (fall) (Figure 6c). Meanwhile, for stratiform rainfall under BR03 (BR03_S), the mean KE_{time} was largest (smallest) at 28.590 (21.558) J m^{-2} h^{-1} in summer (spring) (Figure 6e); for convective rainfall under BR03 (BR03_C), the mean KE_{time} was 379.887 (325.083) J m^{-2} h^{-1} in summer (spring) (Figure 6g). Furthermore, for BR09_S (BR09_C), the mean KE_{mm} (purple solid line) was largest at 11.677 (32.209) J m^{-2} mm^{-1} in summer and smallest at 9.566 (29.265) J m^{-2} mm^{-1} in spring (Figure 6b,d). For BR03_S (BR03_C), the mean KE_{mm} was largest at 13.342 (24.920) J m^{-2} mm^{-1} in summer, and smallest at 11.425 (21.172) J m^{-2} mm^{-1} in spring (Figure 6f,h). In all seasons, for both stratiform and convective rainfall under both BR03 and BR09, summer hadthe largest mean KE_{time} and KE_{mm}.

The scatterplots of KE_{time} vs. R for the entire dataset, and the KE_{time}–R relationship for stratiform and convective rainfall across the seasons under BR09 and BR03 at Zhaosu, are shown in Figure 7. Under BR09_S, the KE_{time}–R relation was revealed as $KE_{time} = 12.837R^{1.173}$ for the entire dataset. In terms of seasons, for the same R, KE_{time} was slightly smaller in spring or fall than that in summer, and KE_{time} was slightly larger in spring than that in fall when $R > 4.0$ mm h^{-1} (Figure 7a). Under BR09_C, the KE_{time}–R relation was $KE_{time} = 23.418R^{1.097}$ for the entire dataset, and the KE_{time}–R relationships were $KE_{time} = 14.433R^{1.229}$, $KE_{time} = 26.543R^{1.065}$, and $KE_{time} = 28.540R^{1.004}$ for spring, summer, and fall, respectively (Figure 7b). Meanwhile, under BR03_S, the KE_{time}–R relationship was $KE_{time} = 11.110R^{1.291}$ for the entire dataset, and the KE_{time}–R relationships were $KE_{time} = 10.374R^{1.327}$, $KE_{time} = 12.030R^{1.252}$, and $KE_{time} = 10.818R^{1.262}$ for spring, summer, and fall, respectively (Figure 7c). Under BR03_C, for the same R, KE_{time} was slightly larger in spring than that in summer for $R > 37.0$ mm h^{-1}, and vice versa when $R < 37.0$ mm h^{-1} (Figure 7d). In summary, the RKEE schemes based on the KE_{time}–R relationships are largely constrained by different classification methods, rainfall types, and seasons.

To further evaluate the accuracy of the derived RKEE schemes across seasons under BR09 and BR03, we compared the KE_{time} estimated by various RKEE schemes with the KE_{time} directly derived from the DSD based on Equation (1). Figure 8 shows the scatterplots of KE_{time} computed from the derived RKEE schemes and KE_{time} computed from DSD with CC, RMSE, and NMAE across seasons under BR09 and BR03. Under BR09_S and BR09_C, the values of CC for the entire dataset and all seasons were >0.93, except for those in fall under BR09_C (0.9085), whereas under BR03_S, the values of CC for the entire dataset and all seasons were <0.90, except for those in summer (0.9101). Furthermore, the performance of the RKEE schemes of KE_{time} for the entire data and all seasons under BR03_C was superior to those under BR03_S, characterized by a larger CC (>0.94) and a smaller NMAE (<0.24 J m^{-2} h^{-1}); the larger RMSE under BR03_C was mainly caused by the larger KE_{time} across seasons, as shown in Figure 6g. More importantly, from a seasonal perspective, under BR09_S, BR09_C, and BR03_S, the performance of KE_{time} in summer was superior to that in other seasons, characterized by a larger CC and a smaller NMAE, while under BR03_C, the performance of KE_{time} in spring was superior to that in summer.

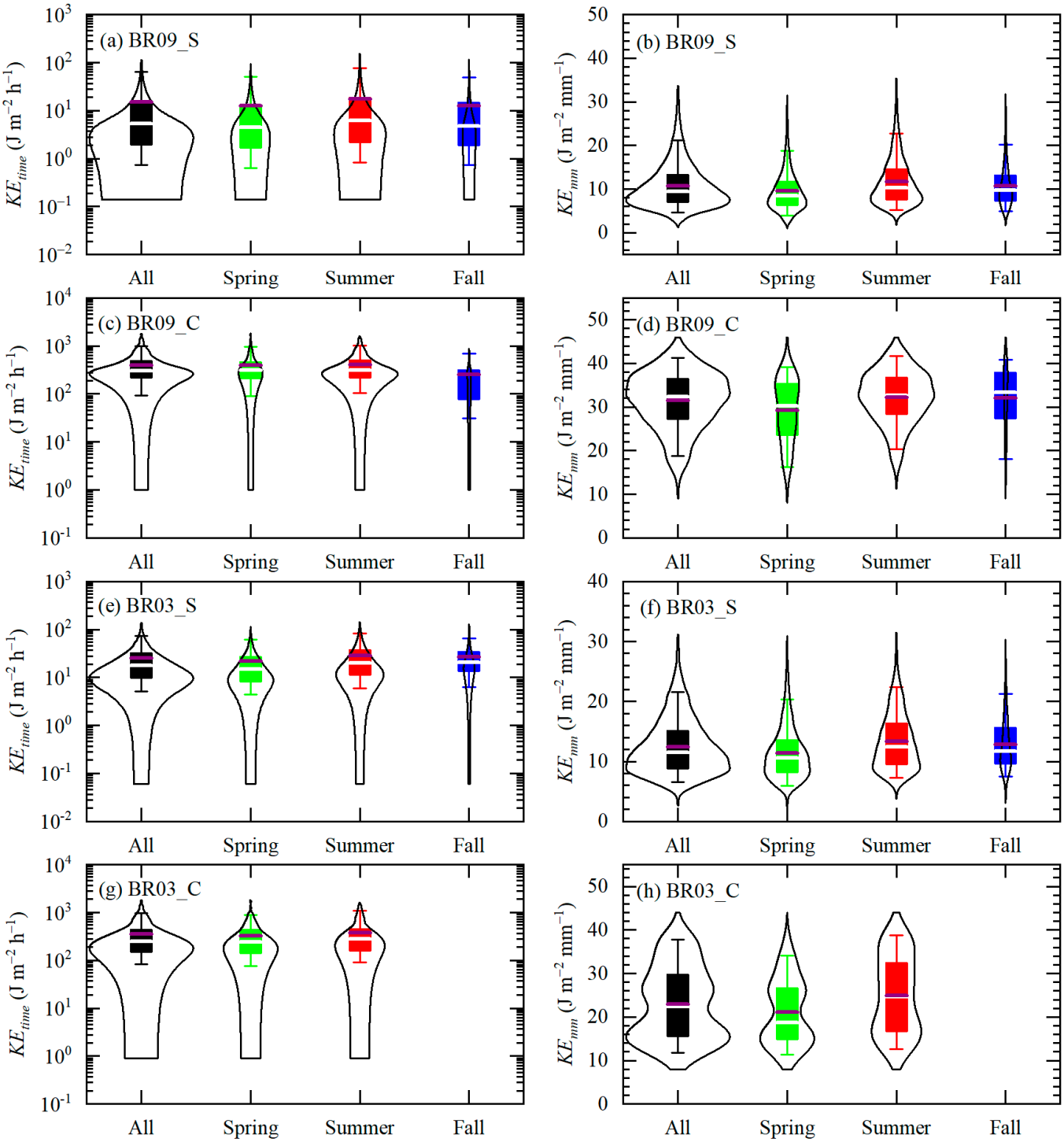

Figure 6. Violin plots of seasonal variations in KE_{time} under (**a**) BR09_S, (**c**) BR09_C, (**e**) BR03_S, and (**g**) BR03_C, and violin plots of seasonal variations in KE_{mm} under (**b**) BR09_S, (**d**) BR09_C, (**f**) BR03_S, and (**h**) BR03_C at Zhaosu.

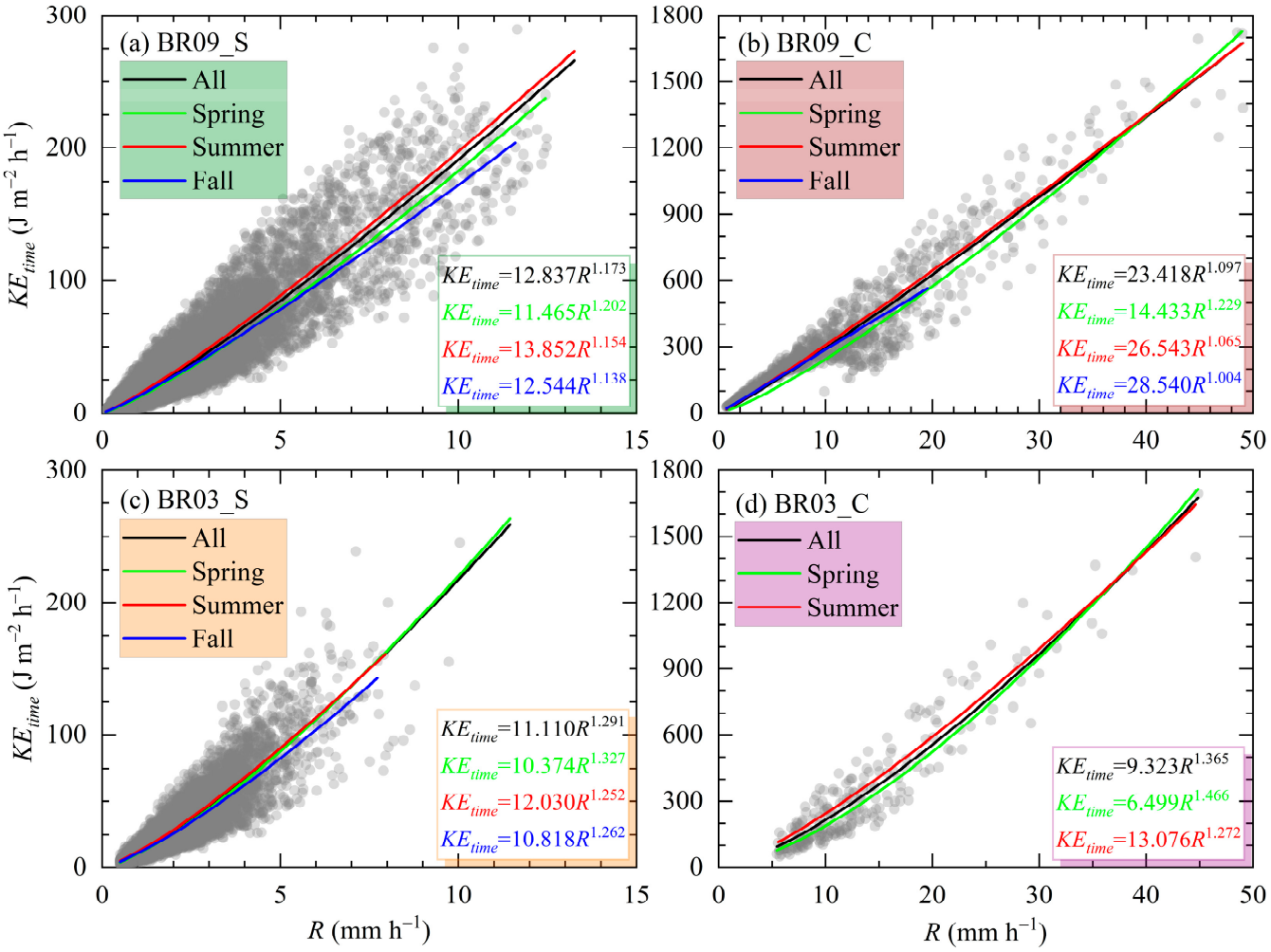

Figure 7. Scatterplots of KE_{time} vs. R for the entire data and the seasonal variation of the fitted KE_{time}–R relationship at Zhaosu under (**a**) BR09_S, (**b**) BR09_C, (**c**) BR03_S, and (**d**) BR03_C.

Scatterplots of KE_{mm} vs. D_m for the entire dataset and seasonal variation in the KE_{mm}–D_m relationship for different rainfall types under BR09 and BR03 are shown in Figure 9. Under BR09_S, for the entire data, the KE_{mm}–D_m relationship was $KE_{mm} = -1.81D_m^2 + 20.91D_m - 8.35$. In terms of seasons, when $D_m > 2.2$ mm, KE_{mm} was slightly larger in spring than that in summer and fall (Figure 9a). Under BR09_C, for the entire dataset, the KE_{mm}–D_m relationship was $KE_{mm} = -2.20D_m^2 + 21.49D_m - 8.39$, and the seasonal variation in the KE_{mm}–D_m relationship was insignificant compared to that under BR09_S (Figure 9b). Meanwhile, under BR03_S, the KE_{mm}–D_m relationship was $KE_{mm} = -2.60D_m^2 + 23.59D_m - 10.15$ for the entire data, and the KE_{mm}–D_m relationships across the seasons were $KE_{mm} = -2.57D_m^2 + 23.53D_m - 10.07$, $KE_{mm} = -2.73D_m^2 + 23.96D_m - 10.44$, and $KE_{mm} = -2.48D_m^2 + 23.59D_m - 10.23$, respectively (Figure 9c). Under BR03_C, the KE_{mm}–D_m relationship was $KE_{mm} = -2.60D_m^2 + 23.37D_m - 10.38$ for the entire dataset, and the KE_{mm}–D_m relationship across the seasons was insignificant compared to that under BR03_S (Figure 9d). In summary, RKEE schemes based on KE_{mm}–D_m relationships were largely constrained by different rainfall types and their classification methods. In addition, the KE_{mm}–D_m relationship across the seasons during stratiform rainfall was more pronounced than that during convective rainfall.

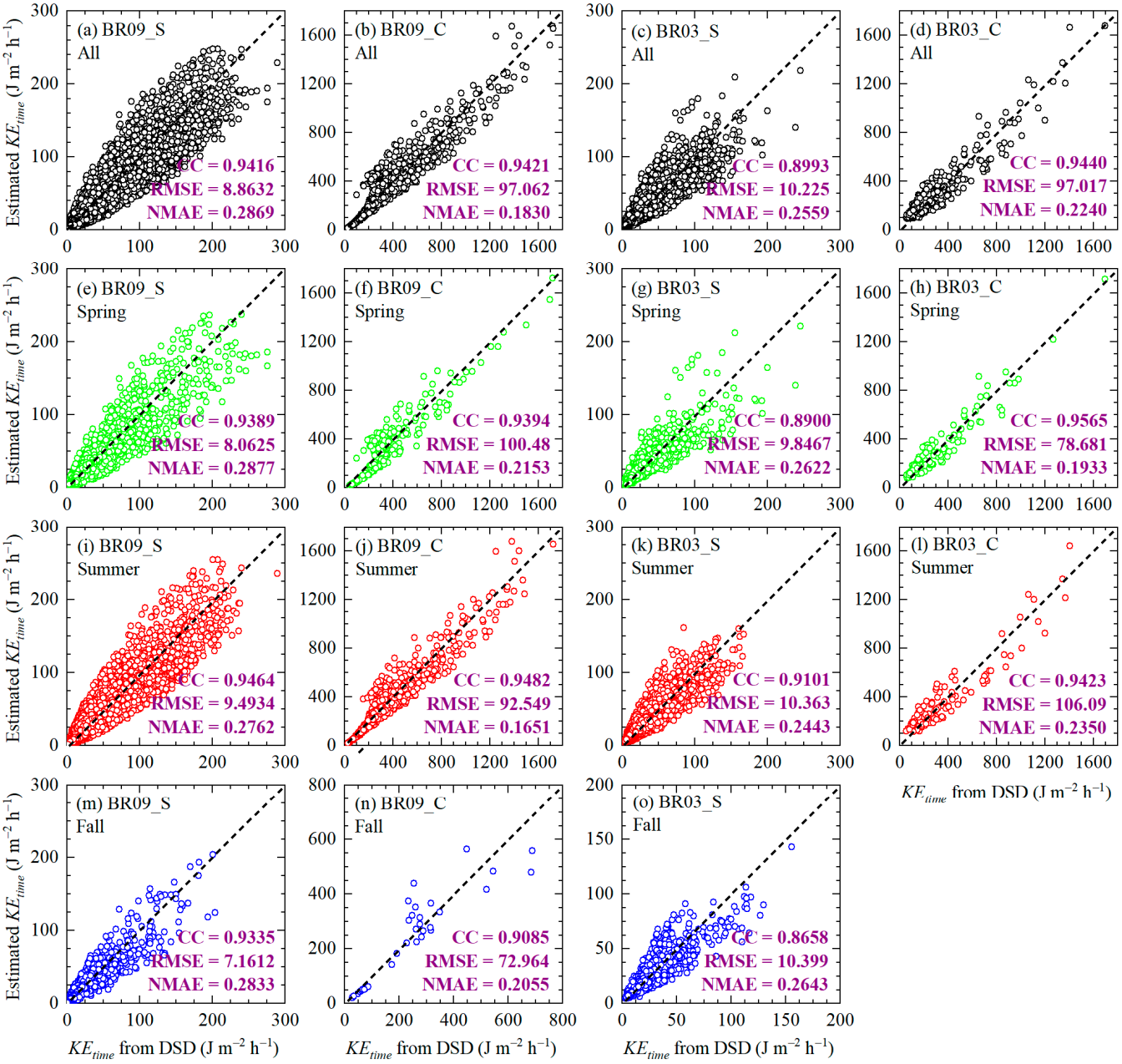

Figure 8. Scatterplot of estimated KE_{time} from RKEE schemes versus KE_{time} calculated from DSD for (**a**) the entire data, (**e**) spring, (**i**) summer, and (**m**) fall under BR09_S; those for (**b**) the entire data, (**f**) spring, (**j**) summer, and (**n**) fall under BR09_C; those for (**c**) the entire data, (**g**) spring, (**k**) summer, and (**o**) fall under BR03_S; and those for (**d**) the entire data, (**h**) spring, and (**l**) summer under BR03_C at Zhaosu. Black dashed lines represent the 1:1 relationship.

To further evaluate the accuracy of the derived RKEE schemes across seasons in BR09 and BR03, we compared the estimated KE_{mm} using various RKEE schemes with the KE_{mm} directly derived from the DSD based on Equation (2). Figure 10 shows the scatterplots of KE_{mm} computed from the derived RKEE schemes and KE_{mm} computed from DSD with CC, RMSE, and NMAE for the different rainfall types under BR09 and BR03. All RKEE schemes listed in Figure 10 had excellent performance, characterized by large a CC (>0.99) and a small NMAE (<0.05 J m^{-2} mm^{-1}) and RMSE (<0.60 J m^{-2} mm^{-1}), but there were also some differences between these RKEE schemes. Specifically, the performance of the RKEE schemes of KE_{mm} for all data and seasons under BR09_C (BR03_C) was superior to that under BR09_S (BR03_S), which was characterized by more clustered scatterers along

the 1:1 line, a larger CC, and smaller a NMAE and RMSE. In addition, under BR09_S and BR03_S, the performance of the RKEE schemes of KE_{mm} in summer was superior to that in other seasons, with a larger CC and smaller NMAE and RMSE.

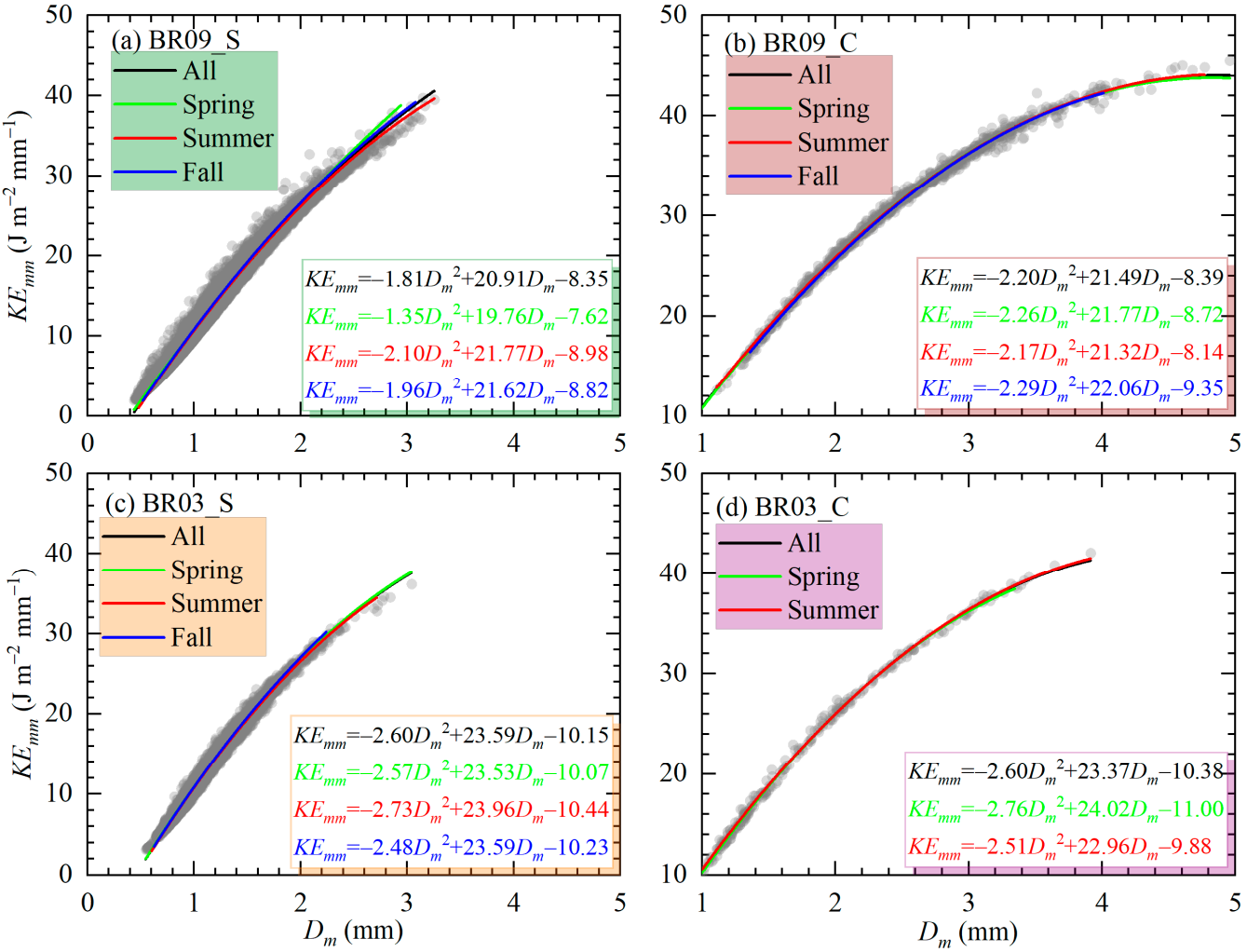

Figure 9. Scatterplots of KE_{mm} vs. D_m for the entire data and the fitted KE_{mm}–D_m relationship across seasons at Zhaosu under (**a**) BR09_S, (**b**) BR09_C, (**c**) BR03_S, and (**d**) BR03_C.

Overall, for both the entire sample and samples of different rainfall types, obtaining KE_{mm} based on D_m (KE_{mm}–D_m relation) was more accurate than obtaining KE_{time} based on R (KE_{time}–R relation). However, it was worth noting that R is easier to obtain than D_m, as the former can be obtained through various methods including observations from widely distributed meteorological stations. In addition, many reanalysis datasets and satellite products also included R. Therefore, obtaining KE_{time} through the KE_{time}–R relation was easier and more convenient, and had a broader application space in the future.

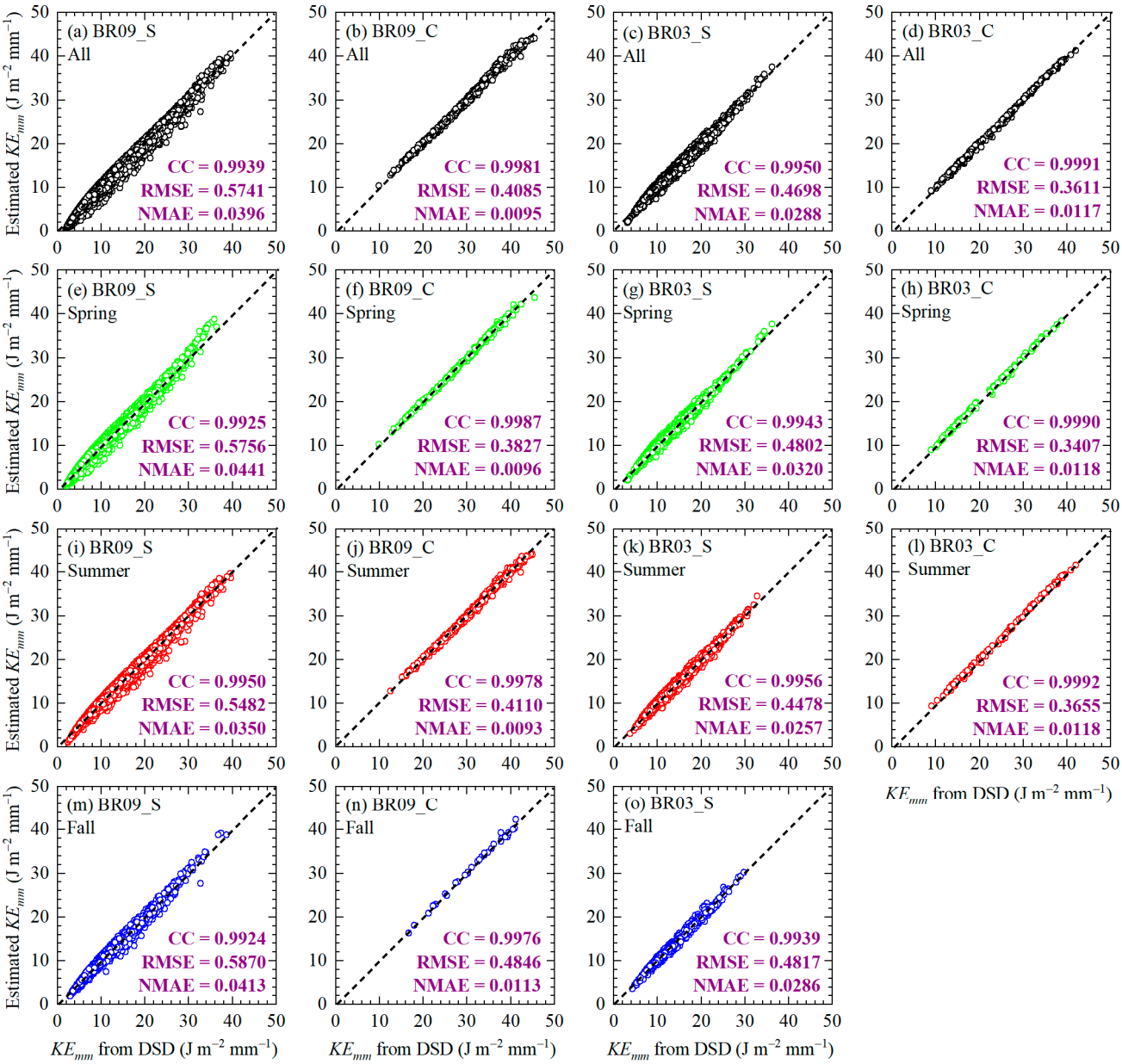

Figure 10. Scatterplot of estimated KE_{mm} from RKEE schemes versus KE_{mm} calculated from DSD for (**a**) the entire data, (**e**) spring, (**i**) summer, and (**m**) fall under BR09_S; for (**b**) the entire data, (**f**) spring, (**j**) summer, and (**n**) fall under BR09_C; for (**c**) the entire data, (**g**) spring, (**k**) summer, and (**o**) fall under BR03_S; and for (**d**) the entire data, (**h**) spring, and (**l**) summer under BR03_C at Zhaosu. Black dashed lines represent the 1:1 relationship.

3.3. Seasonal Variation of Dual-Polarization Radar QPE

Previous studies have revealed that using the method of T-matrix scattering with DSD information to obtain the dual-polarization radar variables Z_h, Z_{dr}, and K_{dp} according to Equations (9)–(11) is reliable and accurate [13,26,27,29–32,56,60]. Figure 11 shows the seasonal variations in the distributions of dual-polarization radar variables Z_h, Z_{dr}, and K_{dp} at Zhaosu. For the entire data and three seasons (spring, summer, fall), the peak distribution of Z_h was ~19.0 dBZ, with mean values (gray solid line) close to ~21.6, ~20.4, ~22.7, and ~20.9 dBZ, respectively (Figure 11a). Z_{dr}'s highest distributions for the entire dataset and three seasons were 0.11, 0.09, 0.13, and 0.13 dB, respectively, and the mean value of Z_{dr} (gray solid line) was largest in summer (0.388 dB) and smallest in spring (0.269 dB) (Figure 11b). For fall, K_{dp} was mostly distributed around 0.007 ° km^{-1}, while for other seasons, the

peak distribution of K_{dp} was 0.011 ° km^{-1}; the mean K_{dp} (gray solid line) was the smallest (largest) in fall (summer) at 0.029 (0.070) ° km^{-1} (Figure 11c).

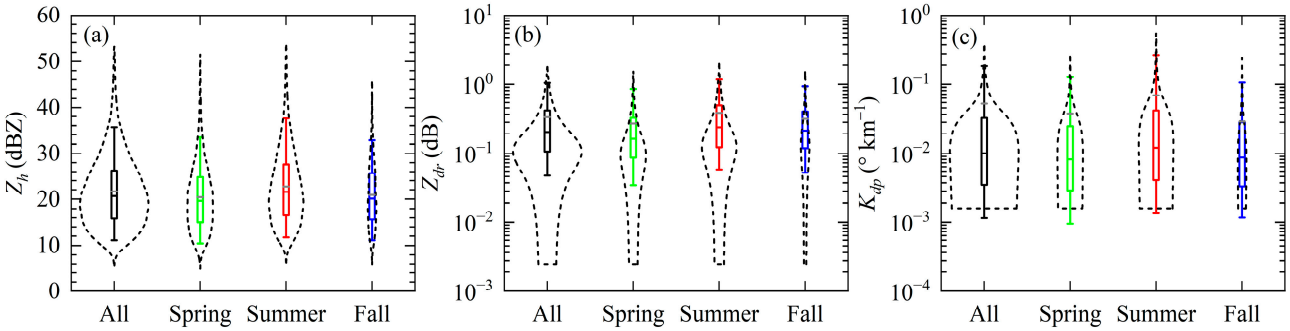

Figure 11. Seasonal variations in the distributions of (**a**) Z_h, (**b**) Z_{dr}, and (**c**) K_{dp} at Zhaosu.

The dual-polarization radar QPE algorithms (single-parameter algorithms $R(Z_h)$ and $R(K_{dp})$, and double-parameter algorithms $R(Z_h,Z_{dr})$ and $R(K_{dp},Z_{dr})$) across the seasons are listed in Table 1. Discrepancies were observed across the seasons for each of the four types of QPE algorithms. Specifically, the coefficient f (g) of the $R(Z_h)$ algorithm varied from 0.064 (0.491) to 0.072 (0.516) between the seasons. Similarly, for the $R(K_{dp})$ algorithm, the coefficient h (i) varied from 13.097 (0.649) to 14.655 (0.680) between the seasons; for the $R(Z_h,Z_{dr})$ algorithm, the coefficients j, k, and l varied from 0.016 to 0.018, 0.763 to 0.822, and −0.593 to −0.311 across the seasons, respectively. In addition, for the $R(K_{dp},Z_{dr})$ algorithm, the coefficient m varied from 24.184 to 30.789, and the variability of coefficient o (−0.156 to −0.274) was relatively greater than that of coefficient n (0.816 to 0.831) across the seasons.

Table 1. Seasonal variation in DSD-based QPE algorithms of dual-polarization radar at Zhaosu.

	$R(Z_h) = f \times Z_h^{\,g}$		$R(K_{dp}) = h \times K_{dp}^{\,i}$		$R(Z_h,Z_{dr}) = j \times Z_h^{\,k} \times 10^{l \times Zdr}$			$R(K_{dp},Z_{dr}) = m \times K_{dp}^{\,n} \times 10^{o \times Zdr}$		
	f	g	h	i	j	k	l	m	n	o
All	0.067	0.504	13.481	0.669	0.018	0.766	−0.345	25.670	0.822	−0.170
Spring	0.067	0.516	14.655	0.666	0.018	0.800	−0.446	30.275	0.827	−0.218
Summer	0.064	0.506	13.097	0.680	0.016	0.763	−0.311	24.184	0.831	−0.156
Fall	0.072	0.491	13.176	0.649	0.018	0.822	−0.593	30.789	0.816	−0.274

Previous studies have shown that evaluating the performance of various dual-polarization radar QPE algorithms based on DSD is important and necessary. R calculated according to Equation (4) was used to evaluate the DSD-based QPE algorithms of the dual-polarization radar [13,30,31,48,56,60,84]. Figure 12 shows the scatterplots of R estimated according to the QPE algorithms and R calculated according to Equation (4) with CC, RMSE, and NMAE across the seasons. For the entire data and all seasons, double-parameter algorithms performed better than single-parameter algorithms with more clustered scatterers on the 1:1 line, larger CC (>0.96), and smaller RMSE (<0.8 mm h^{-1}) and NMAE (<0.23 mm h^{-1}). Moreover, for single-parameter algorithms, regardless of the entire dataset or season, the performance of the $R(K_{dp})$ algorithm was superior to that of the $R(Z_h)$ algorithm. Similarly, for the double-parameter schemes, the $R(K_{dp}, Z_{dr})$ algorithm performed better than the $R(Z_h, Z_{dr})$ algorithm. In addition, both single-parameter algorithms performed the worst in fall, the $R(Z_h, Z_{dr})$ algorithm performed the worst in summer, and the $R(K_{dp}, Z_{dr})$ algorithm showed little difference in performance across seasons.

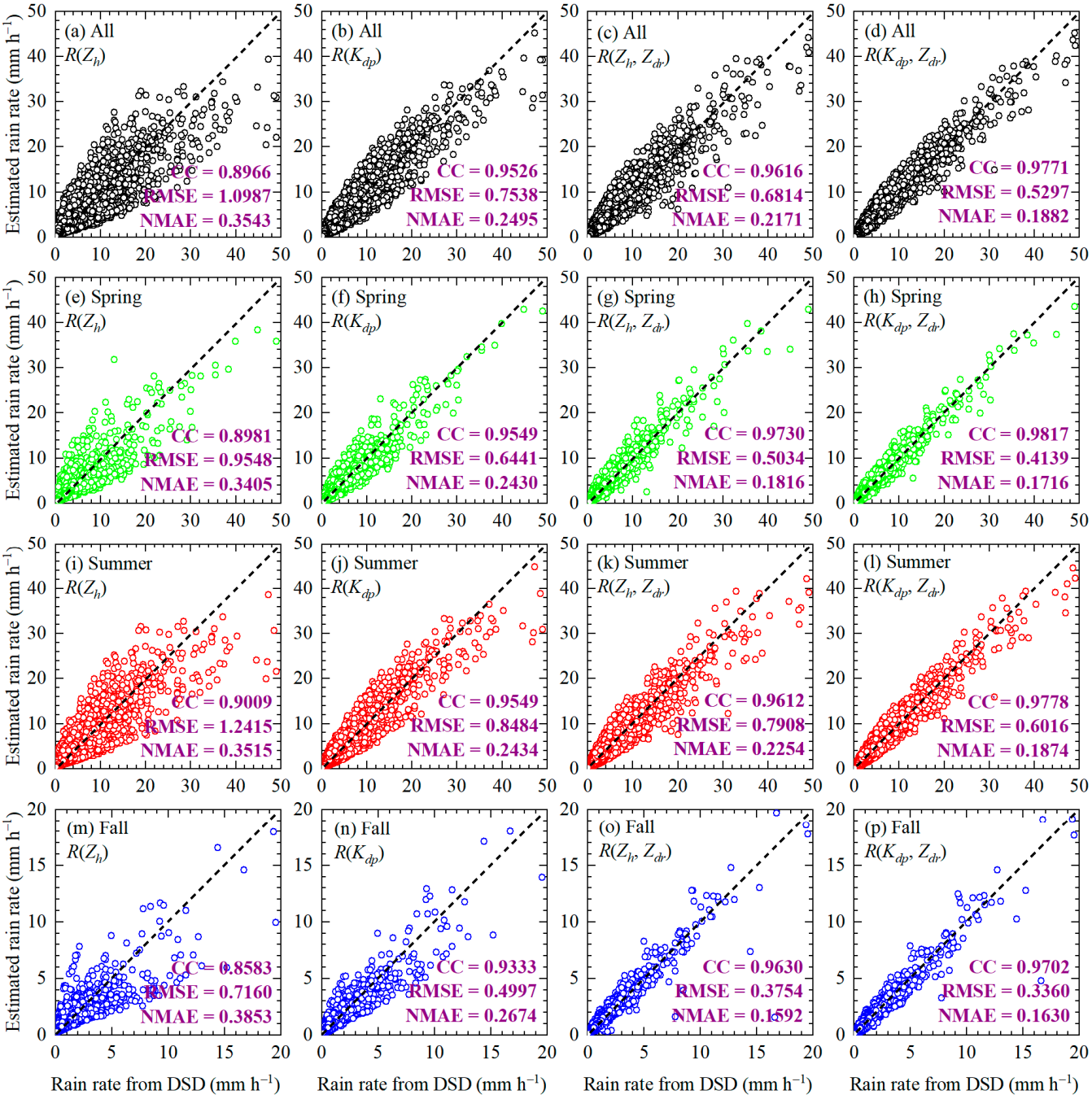

Figure 12. Scatterplot of estimated R based on the $R(Z_h)$ algorithm for (**a**) the entire data, (**e**) spring, (**i**) summer, and (**m**) fall; estimated R based on the $R(K_{dp})$ algorithm for (**b**) the entire data, (**f**) spring, (**j**) summer, and (**n**) fall; estimated R based on the $R(Z_h,Z_{dr})$ algorithm for (**c**) the entire data, (**g**) spring, (**k**) summer, and (**o**) fall; and estimated R based on the $R(K_{dp},Z_{dr})$ algorithm for (**d**) the entire data, (**h**) spring, (**l**) summer, and (**p**) fall versus calculated R according to Equation (4) at Zhaosu. Black dashed lines represent the 1:1 relationship.

3.4. Seasonal Variation of Dual-Polarization Radar QPE for Different Rainfall Types

Figure 13 shows the seasonal variations in the distributions of the dual-polarization radar variables Z_h, Z_{dr}, and K_{dp} for stratiform and convective rainfall under BR09 and BR03 at Zhaosu. For BR09_S, Z_h with the highest distribution across the seasons was ~19.0 dBZ, and the mean Z_h (gray solid line) was largest (smallest) at 22.01 (20.11) J m^{-2} h^{-1} in summer (spring) (Figure 13a). For BR09_C, the peak distribution of Z_h was ~42.5 dBZ, and the

mean Z_h was largest at 44.73 dBZ (smallest at 42.05 dBZ) in summer (fall) (Figure 13d). Meanwhile, for BR03_S, the mean Z_h was largest at 27.32 dBZ (smallest at 25.52 dBZ) in summer (spring) (Figure 13g), and for BR03_C, the mean Z_h was 41.96 dBZ (40.23 dBZ) in summer (spring) (Figure 13j). Furthermore, for BR09_S (BR09_C), Z_{dr} with the highest distribution across the seasons was ~0.1 (1.4) dB and the mean Z_{dr} (gray solid line) was largest at 0.34 (1.81) dB in summer (fall), and smallest at 0.25 (1.56) dB in spring (Figure 13b,e). For BR03_S (BR03_C), the mean Z_{dr} was largest at 0.45 (1.22) dB in summer, and the smallest at 0.35 (0.93) dB in spring (Figure 13h,k). In addition, for BR09_S (BR09_C), the peak distribution of K_{dp} was ~0.006 (0.65) ° km^{-1}, and the mean value of K_{dp} (gray solid line) was close to ~0.031 (1.085), ~0.025 (1.034), ~0.037 (1.123), and ~0.025 (0.677) ° km^{-1} for the entire data, spring, summer and fall, respectively (Figure 13c,f). For BR03_S (BR03_C), the mean K_{dp} was the largest at 0.058 (1.003) ° km^{-1} in summer and the smallest at 0.042 (0.798) ° km^{-1} in spring (Figure 13i,l).

The dual-polarization radar QPE algorithms for stratiform and convective rainfall under BR09 across seasons based on the DSD information at Zhaosu are listed in Table 2. The coefficient f(g) of the $R(Z_h)$ algorithm varied from 0.054 (0.524) to 0.063 (0.535) between different seasons for BR09_S, while the coefficient f (g) of the $R(Z_h)$ algorithm varied from 0.054 (0.451) to 0.102 (0.521) between different seasons for BR09_C. Similarly, for the $R(K_{dp})$ algorithm, the coefficient h(i) varied from 14.318 (0.688) to 15.828 (0.711) across seasons for BR09_S, while the coefficient h(i) varied from 12.098 (0.692) to 14.194 (0.786) across seasons for BR09_C. Furthermore, for the $R(Z_h,Z_{dr})$ algorithm, the coefficients j, k, and l varied from 0.013 to 0.016, 0.852 to 0.877, and −0.653 to −0.680 across seasons for BR09_S, respectively, while the coefficients j, k, and l varied from 0.006 to 0.048, 0.615 to 0.837, and −0.225 to −0.367 across seasons for BR09_C, respectively. In addition, for the $R(K_{dp},Z_{dr})$ algorithm, the differences in the coefficients m, n, and o across seasons during convective rainfall were greater than those during stratiform rainfall.

Table 2. Seasonal variation of the DSD-based QPE algorithms of a dual-polarization radar for different rainfall types under BR09 at Zhaosu.

	$R(Z_h) = f \times Z_h^g$		$R(K_{dp}) = h \times K_{dp}^i$		$R(Z_h,Z_{dr}) = j \times Z_h^k \times 10^{l \times Zdr}$			$R(K_{dp},Z_{dr}) = m \times K_{dp}^n \times 10^{o \times Zdr}$		
BR09_S	f	g	h	i	j	k	l	m	n	o
All	0.060	0.521	14.640	0.690	0.014	0.867	−0.675	38.775	0.864	−0.370
Spring	0.063	0.524	15.717	0.688	0.015	0.858	−0.653	38.710	0.853	−0.352
Summer	0.056	0.525	14.318	0.699	0.013	0.877	−0.680	38.794	0.876	−0.370
Fall	0.054	0.535	15.828	0.711	0.016	0.852	−0.669	37.766	0.849	−0.372
BR09_C	f	g	h	i	j	k	l	m	n	o
All	0.067	0.504	12.591	0.762	0.009	0.808	−0.291	22.139	0.894	−0.144
Spring	0.097	0.482	14.194	0.703	0.018	0.772	−0.367	26.876	0.849	−0.186
Summer	0.054	0.521	12.098	0.786	0.006	0.837	−0.277	20.926	0.919	−0.135
Fall	0.102	0.451	12.127	0.692	0.048	0.615	−0.225	17.978	0.763	−0.102

Figures 14 and 15 show scatterplots of estimated R based on QPE algorithms and calculated R according to Equation (4) with respect to CC, RMSE, and NMAE for BR09_S and BR09_C across the seasons. For both stratiform and convective rainfall, and for both the entire data and all seasons, double-parameter algorithms were superior to single-parameter algorithms, with more clustered scatterers along the 1:1 line, a larger CC, and a smaller RMSE and NMAE, except for the $R(K_{dp}, Z_{dr})$ algorithm in the fall under BR09_C. Moreover, the $R(K_{dp})$ algorithm was superior to the $R(Z_h)$ algorithm for both BR09_S and BR09_C across seasons. Meanwhile, the performance of the $R(Z_h, Z_{dr})$ algorithm was better than that of the $R(K_{dp}, Z_{dr})$ algorithm for BR09_S in spring and fall, whereas the opposite was true for the BR09_C in all seasons. Similarly, seasonal variations in the various QPE algorithms cannot be ignored. For example, for BR09_C, the single-parameter algorithms performed the best (worst) in summer (fall) and the $R(Z_h, Z_{dr})$ algorithm performed the best (worst) in

spring (fall), whereas for BR09_S, the $R(K_{dp}, Z_{dr})$ algorithm performed the best (worst) in summer (spring).

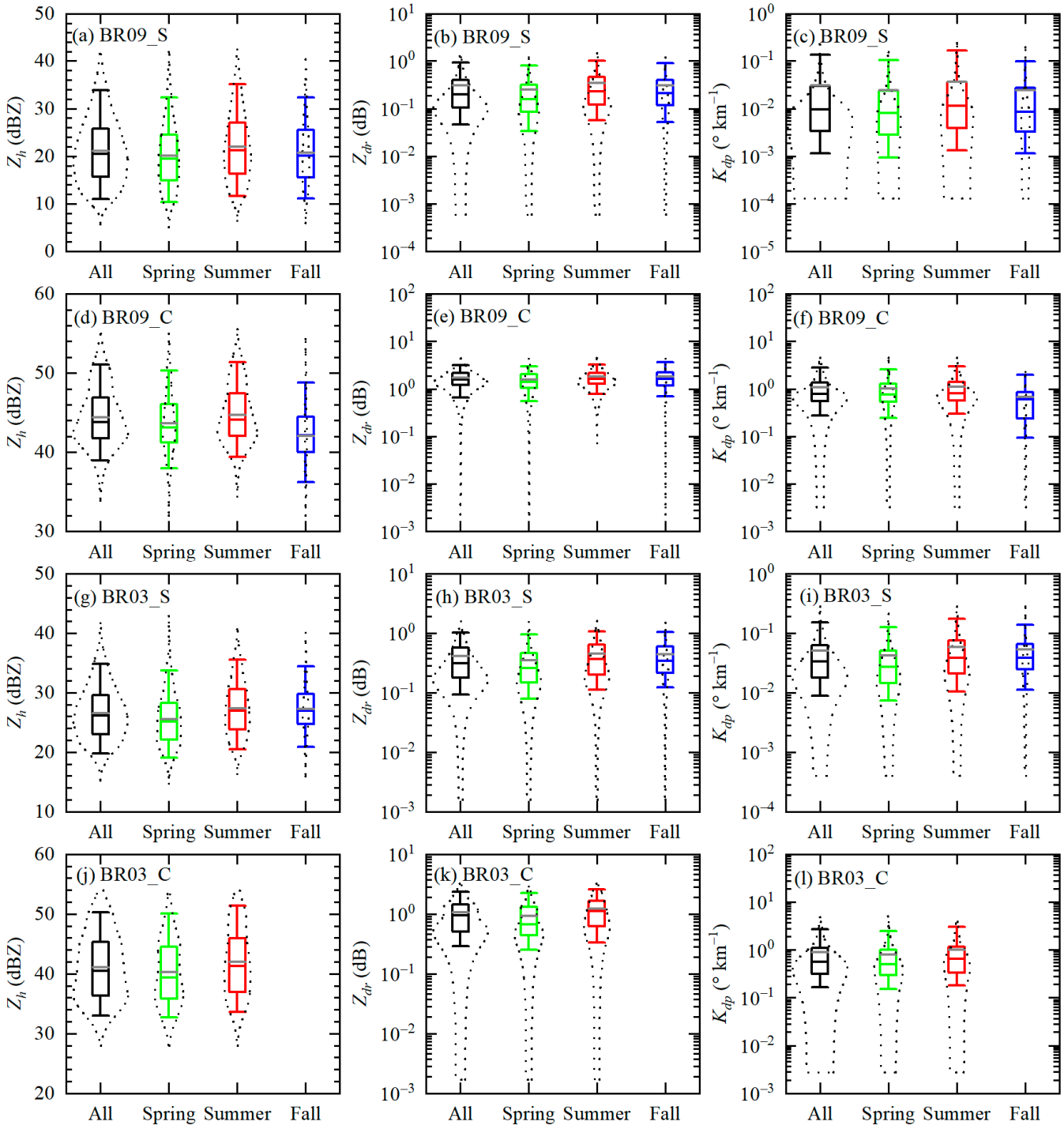

Figure 13. Seasonal variations in the distributions of Z_h under (**a**) BR09_S, (**d**) BR09_C, (**g**) BR03_S, and (**j**) BR03_C; those of Z_{dr} under (**b**) BR09_S, (**e**) BR09_C, (**h**) BR03_S, and (**k**) BR03_C; and those of K_{dp} under (**c**) BR09_S, (**f**) BR09_C, (**i**) BR03_S, and (**l**) BR03_C at Zhaosu.

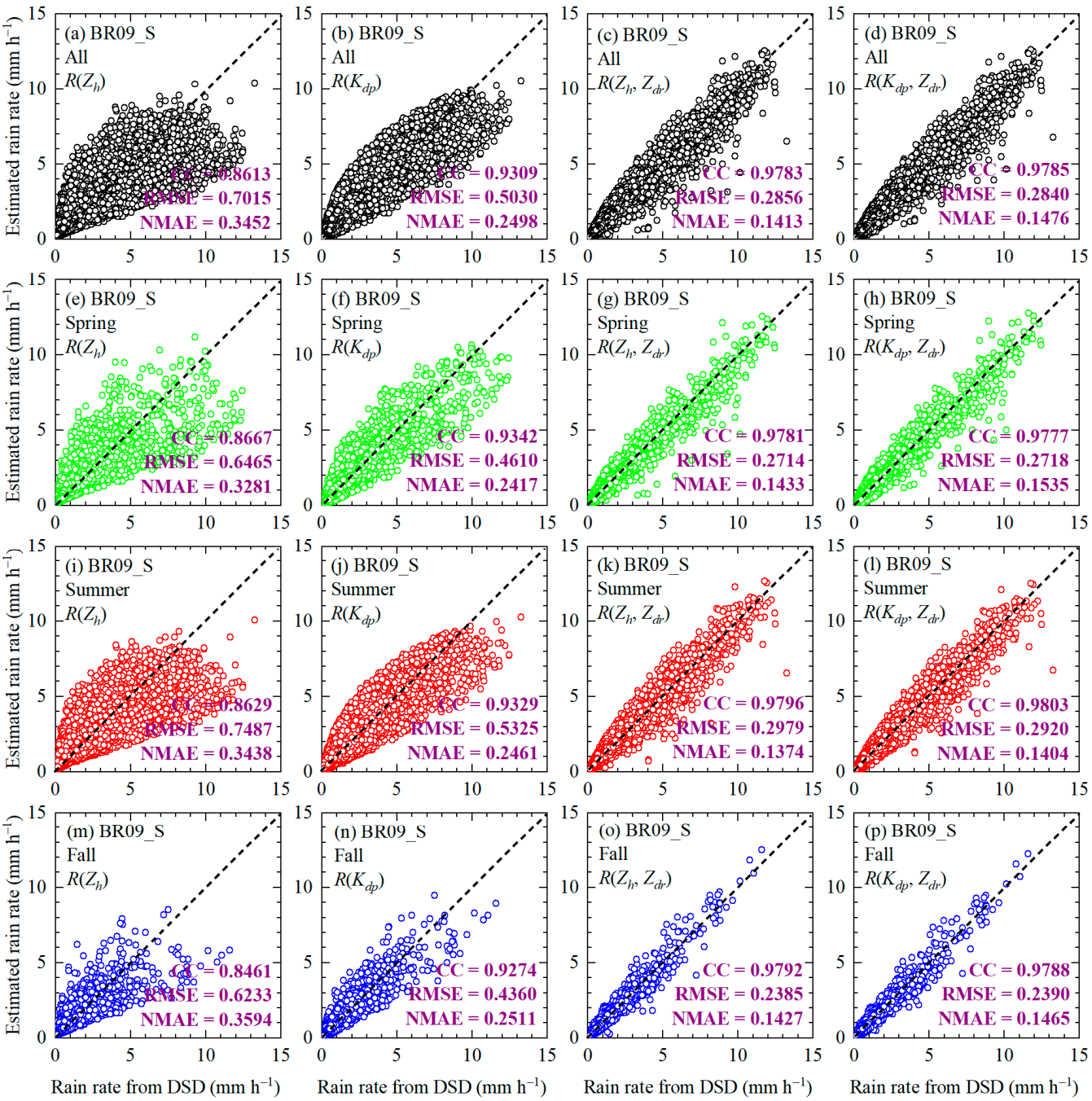

Figure 14. Scatterplot of estimated R based on the $R(Z_h)$ algorithm during BR09_S for (**a**) the entire data, (**e**) spring, (**i**) summer, and (**m**) fall; that based on the $R(K_{dp})$ algorithm during BR09_S for (**b**) the entire data, (**f**) spring, (**j**) summer, and (**n**) fall; that based on the $R(Z_h,Z_{dr})$ algorithm during BR09_S for (**c**) the entire data, (**g**) spring, (**k**) summer, and (**o**) fall; and that based on the $R(K_{dp},Z_{dr})$ algorithm during BR09_S for (**d**) the entire data, (**h**) spring, (**l**) summer, and (**p**) fall versus calculated R according to Equation (4) at Zhaosu. Black dashed lines represent the 1:1 relationship.

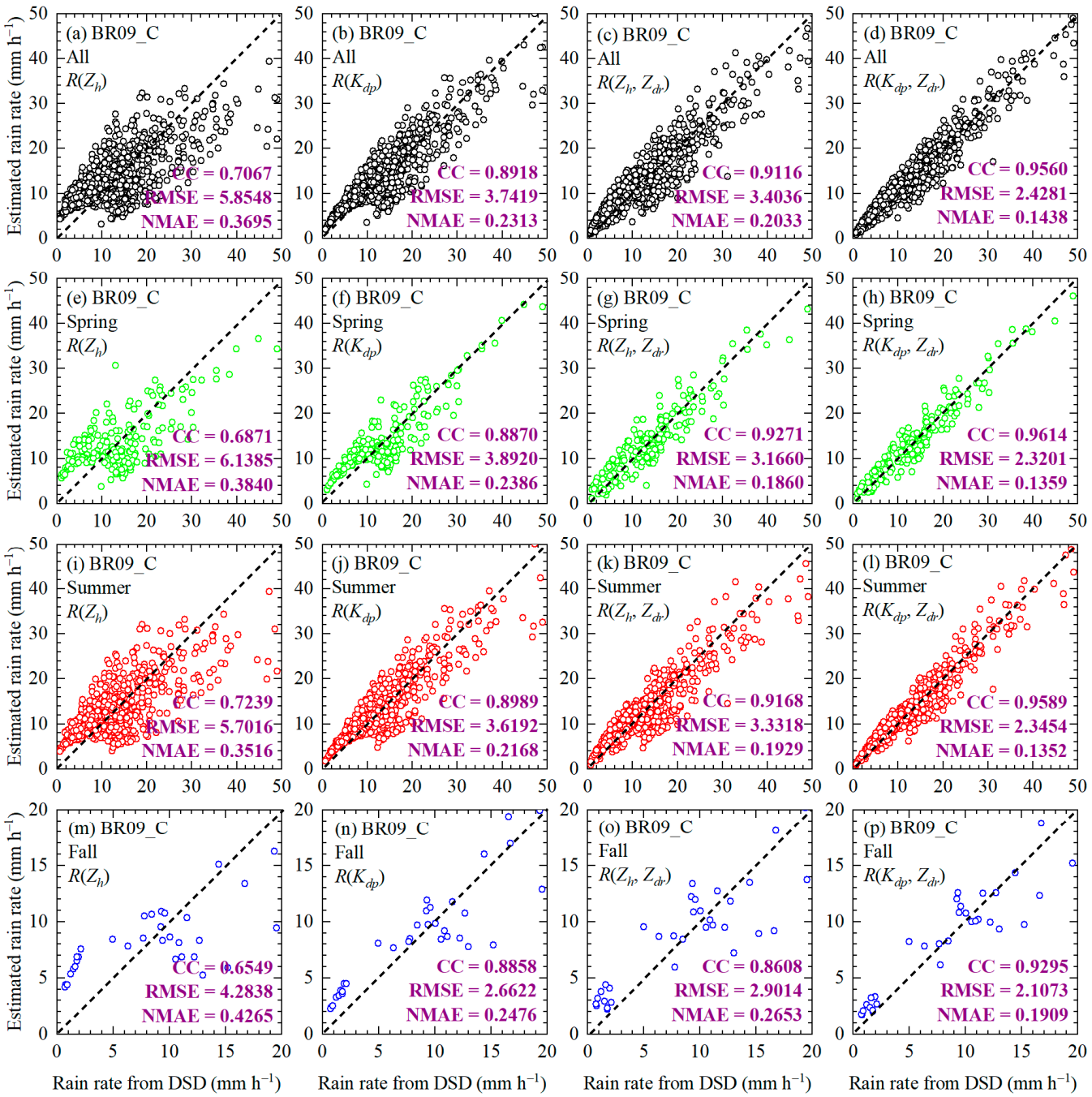

Figure 15. Scatterplot of estimated R based on the $R(Z_h)$ algorithm during BR09_C for (**a**) the entire data, (**e**) spring, (**i**) summer, and (**m**) fall; that based on the $R(K_{dp})$ algorithm during BR09_C for (**b**) the entire data, (**f**) spring, (**j**) summer, and (**n**) fall; that based on the $R(Z_h,Z_{dr})$ algorithm during BR09_C for (**c**) the entire data, (**g**) spring, (**k**) summer, and (**o**) fall; and that based on the $R(K_{dp},Z_{dr})$ algorithm during BR09_C for (**d**) the entire data, (**h**) spring, (**l**) summer, and (**p**) fall versus calculated R according to Equation (4) at Zhaosu. Black dashed lines represent the 1:1 relationship.

Similar to Table 2, the dual-polarization radar QPE algorithms for stratiform and convective rainfall under BR03 across seasons based on the DSD information at Zhaosu are listed in Table 3. The coefficient $f(g)$ of the $R(Z_h)$ algorithm varied from 0.126 (0.391) to 0.158 (0.418) between different seasons for BR03_S, while the coefficient $f(g)$ of the $R(Z_h)$ algorithm varied from 0.417 (0.346) to 0.506 (0.350) between different seasons for BR03_C. Similarly, for the $R(K_{dp})$ algorithm, the coefficient $h(i)$ varied from 10.830 (0.558) to 11.653

(0.597) across seasons for BR03_S, while the coefficient $h(i)$ varied from 14.936 (0.530) to 16.909 (0.571) across seasons for BR03_C. Furthermore, for the $R(Z_h,Z_{dr})$ algorithm, the coefficients j, k, and l varied from 0.015 to 0.019, 0.824 to 0.859, and −0.622 to −0.655 across the seasons for BR03_S, respectively, while the coefficients j, k, and l varied from 0.032 to 0.066, 0.627 to 0.696, and −0.273 to −0.280 across the seasons for BR03_C, respectively. Similarly, for the $R(K_{dp},Z_{dr})$ algorithm, differences were observed for the different seasons and rainfall types.

Table 3. Seasonal variation of QPE algorithms of DSD-based dual-polarization radar for different rainfall types under BR03 at Zhaosu.

	$R(Z_h) = f \times Z_h^{\,g}$		$R(K_{dp}) = h \times K_{dp}^{\,i}$		$R(Z_h,Z_{dr}) = j \times Z_h^{\,k} \times 10^{l \times Zdr}$			$R(K_{dp},Z_{dr}) = m \times K_{dp}^{\,n} \times 10^{o \times Zdr}$		
BR03_S	f	g	h	i	j	k	l	m	n	o
All	0.142	0.403	11.178	0.575	0.017	0.842	−0.641	36.243	0.837	−0.345
Spring	0.154	0.391	10.830	0.558	0.017	0.835	−0.622	35.616	0.829	−0.329
Summer	0.126	0.418	11.580	0.597	0.015	0.859	−0.655	37.503	0.855	−0.353
Fall	0.158	0.394	11.653	0.577	0.019	0.824	−0.644	35.790	0.820	−0.357
BR03_C	f	g	h	i	j	k	l	m	n	o
All	0.526	0.335	15.942	0.539	0.046	0.662	−0.281	25.984	0.776	−0.155
Spring	0.506	0.346	16.909	0.530	0.066	0.627	−0.273	25.102	0.714	−0.137
Summer	0.417	0.350	14.936	0.571	0.032	0.696	−0.280	26.054	0.831	−0.164

Similar to Figures 14 and 15, the scatterplots of R estimated R based on QPE algorithms and calculated R according to Equation (4) with respect to CC, RMSE, and NMAE for BR03_S and BR03_C across seasons; these scatterplots are shown in Figures 16 and 17. For the entire data and all seasons, the performance of the double-parameter algorithms was superior to that of the single-parameter algorithms for both BR03_S and BR03_C. Moreover, for both BR03_S and BR03_C in all seasons, the $R(K_{dp})$ algorithm was superior to the $R(Z_h)$ algorithm. In addition, the performance of the $R(K_{dp}, Z_{dr})$ algorithm was superior to that of the $R(Z_h, Z_{dr})$ algorithm for BR03_C, whereas the difference between the two algorithms was very small for BR03_S. Seasonal variations in the performance of each QPE algorithm are shown in Figures 16 and 17. For BR03_C, both the double-parameter and single-parameter algorithms performed better in spring than in summer. For BR03_S, double-parameter algorithms performed the best in summer with larger CC (>0.96) and smaller NMAE (<0.11 mm h^{-1}).

Overall, for both the entire sample and samples of different rainfall types, obtaining R based on $R(K_{dp})$ [$R(K_{dp}, Z_{dr})$] relation with K_{dp} was more accurate than obtaining R based on $R(Z_h)$ [$R(Z_h, Z_{dr})$] without K_{dp}, and this feature was more pronounced at higher R in convective rainfall (BR03_C and BR09_C). Meanwhile, in most cases, the double-parameter relations [$R(K_{dp}, Z_{dr})$ and $R(Z_h, Z_{dr})$] were more accurate than the single-parameter relations [$R(K_{dp})$ and $R(Z_h)$]. However, it is worth noting that for the actual dual-polarization radar, K_{dp} was less susceptible to the effects of DSD, partial obstruction, and radar calibration errors compared to Z_h and Z_{dr}. Therefore, in future practical applications, the $R(K_{dp})$ relation may be the best choice, followed by the $R(K_{dp}, Z_{dr})$ relation. In addition, we also emphasized the impact of seasons, rainfall types, and classification methods of rainfall types on the estimation accuracy of R in the Tianshan Mountains.

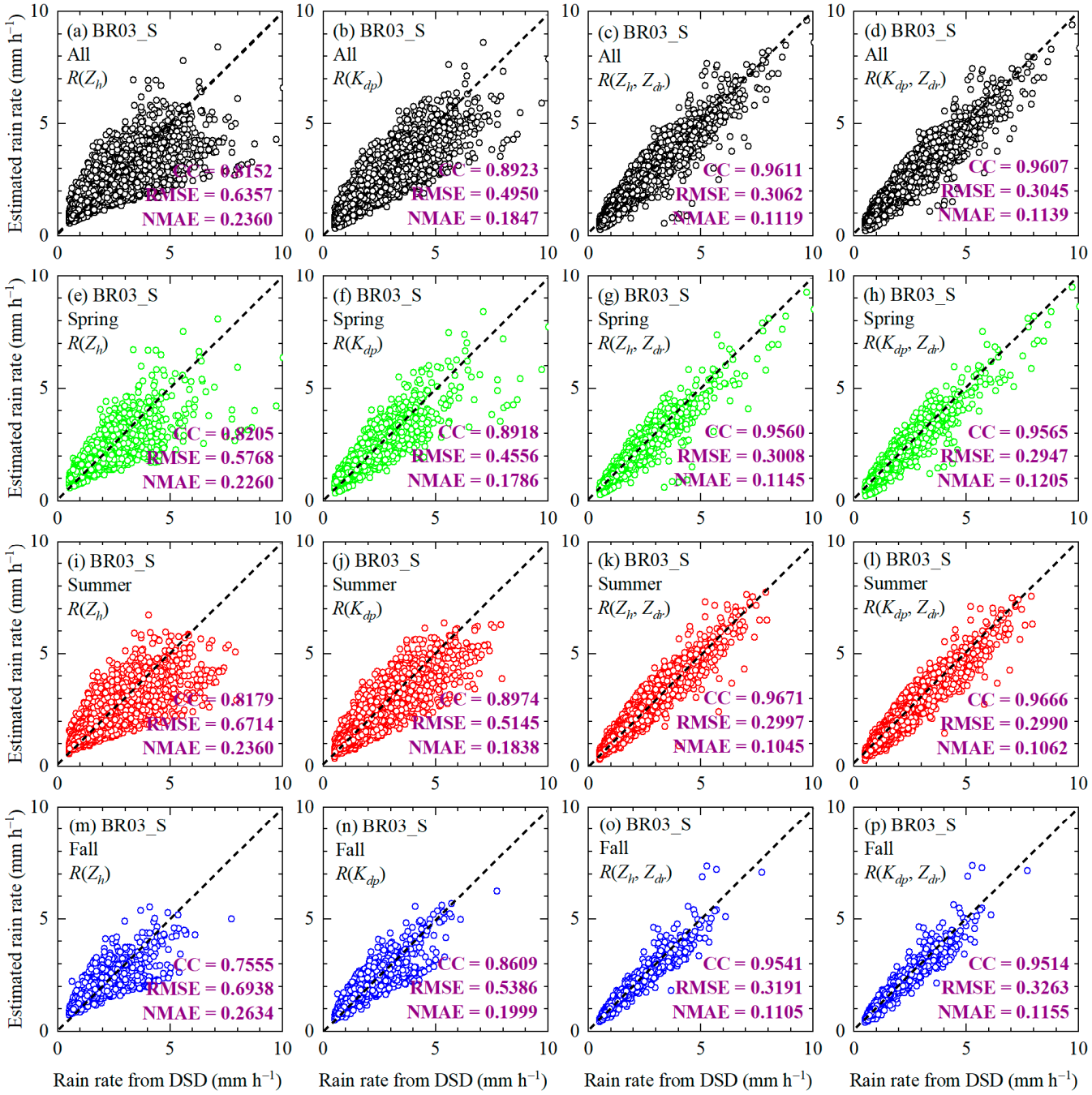

Figure 16. Scatterplot of estimated R based on the $R(Z_h)$ algorithm during BR03_S for (**a**) the entire data, (**e**) spring, (**i**) summer, and (**m**) fall; that based on the $R(K_{dp})$ algorithm during BR03_S for (**b**) the entire data, (**f**) spring, (**j**) summer, and (**n**) fall; that based on the $R(Z_h,Z_{dr})$ algorithm during BR03_S for (**c**) the entire data, (**g**) spring, (**k**) summer, and (**o**) fall; and that based on the $R(K_{dp},Z_{dr})$ algorithm during BR03_S for (**d**) the entire data, (**h**) spring, (**l**) summer, and (**p**) fall versus calculated R according to Equation (4) at Zhaosu. Black dashed lines represent the 1:1 relationship.

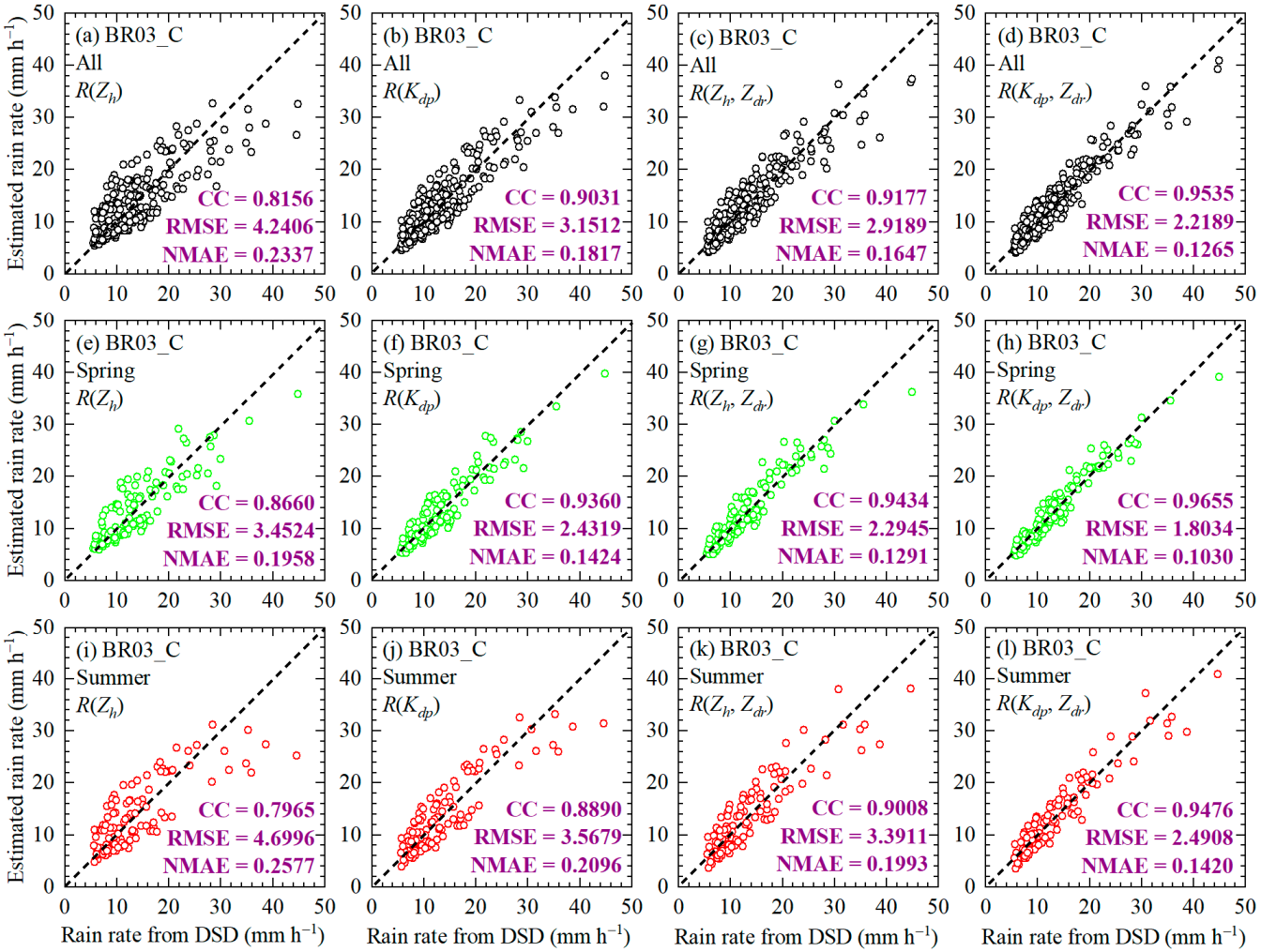

Figure 17. Scatterplot of estimated R based on the $R(Z_h)$ algorithm during BR03_C for (**a**) the entire data, (**e**) spring, and (**i**) summer; that based on the $R(K_{dp})$ algorithm during BR03_C for (**b**) the entire data, (**f**) spring, and (**j**) summer; that based on the $R(Z_h,Z_{dr})$ algorithm during BR03_C for (**c**) the entire data, (**g**) spring, and (**k**) summer; and that based on the $R(K_{dp},Z_{dr})$ algorithm during BR03_C for (**d**) the entire data, (**h**) spring, and (**l**) summer versus calculated R according to Equation (4) at Zhaosu. Black dashed lines represent the 1:1 relationship.

4. Discussion

Affected by various factors such as climate, geographical location, terrain, season, rainfall type, and weather system, DSD exhibits diverse characteristics worldwide [16–23]. The diversity of DSD directly leads to differences in RKEE schemes [9,28,35,36] and QPE algorithms [20–27] derived from DSD, which are also affected by the various factors mentioned above. Secondary disasters such as floods, landslides, and mudslides caused by precipitation are prone to occur near the steep terrain of the Tianshan Mountains [56,57]. However, insufficient attention has been paid to RKEE and QPE in this region. Therefore, this study conducted an in-depth study of the RKEE and dual-polarization radar QPE in the Tianshan Mountains, including seasonal variations and the impacts of different rainfall types (stratiform rainfall and convective rainfall) based on two classic classification methods for rainfall types (BR09 and BR03), as reported by Bringi et al. [62] and Bringi et al. [18], respectively. This study has important theoretical and application value for expanding and deepening our understanding of RKEE and dual-polarization radar QPE in arid areas near mountains. RKEE schemes based on KE_{time}–R relationships are largely constrained by different classification methods, rainfall types, and seasons.

The results of this study demonstrate that RKEE schemes and QPE algorithms of dual-polarization radar are largely constrained by rainfall types, their classification methods, and the seasons in the Tianshan Mountains. Therefore, establishing corresponding REKK schemes and QPE algorithms for a dual-polarization radar according to different rainfall types, their classification methods, and seasons are of great significance to further improve the accuracy of the RKEE and QPE of dual-polarization radar.

However, DSD is highly variable in mountainous areas, and RKEE schemes and dual-polarization radar QPE algorithms derived from DSD also exhibit strong variability, which was partially confirmed in our previous research [57]. Therefore, in the future, it will be necessary to establish a denser DSD observation network to further obtain RKEE schemes and dual-polarization radar QPE algorithms over the Tianshan Mountains at a larger spatial scale. In addition, in steep terrain areas such as the Tianshan Mountains, various satellite observations have important application value for revealing RKEE schemes and dual-polarization radar QPE algorithms over the Tianshan Mountains on a larger scale.

5. Conclusions

To reveal the seasonal variations of the rainfall kinetic energy estimation (RKEE) and the dual-polarization radar quantitative precipitation estimation (QPE) under different rainfall types based on two classic classification methods for rainfall types, defined by Bringi et al. [62] (BR09) and Bringi et al. [18] (BR03) in the Tianshan Mountains, China, the raindrop size distribution (DSD) data from a disdrometer at Zhaosu in the Tianshan Mountains during 2020–2022 were used to derive rainfall kinetic energy (KE_{time} and KE_{mm}) and dual-polarization radar parameters (Z_h, Z_{dr}, and K_{dp}) and establish DSD-based RKEE schemes and QPE algorithms for a dual-polarization radar. The major conclusions are summarized as follows:

(1) Mean KE_{time} was the largest (smallest) at 29.418 (14.006) J m^{-2} h^{-1} in summer (fall), and mean KE_{mm} was the largest (smallest) at 12.307 (9.826) J m^{-2} mm^{-1} in summer (spring). Two RKEE schemes, KE_{time}–R and KE_{mm}–D_m, were established as $KE_{time} = 12.495R^{1.285}$ and $KE_{mm} = -2.260{D_m}^2 + 21.953D_m - 8.899$ for the entire data, respectively, and both showed seasonal variations. By comparing the estimated KE_{time} and KE_{mm} of the established RKEE schemes with the KE_{time} and KE_{mm} obtained directly from DSD based on the CC, RMSE, and NMAE, it was confirmed that the RKEE schemes performed well for the entire dataset and different seasons.

(2) For both stratiform and convective rainfall under both BR03 and BR09 (i.e., BR09_S, BR09_C, BR03_S, and BR03_C), mean KE_{time} (17.535, 405.907, 28.590, and 379.887 J m^{-2} h^{-1}, respectively), and KE_{mm} (11.677, 32.209, 13.342, and 24.920 J m^{-2} mm^{-1}, respectively) in summer were larger than those in other seasons. The KE_{time}–R and KE_{mm}–D_m relationships for stratiform and convective rainfall under BR09 and BR03 were established and showed seasonal variations. The evaluation results showed that both types of RKEE schemes had excellent estimation performances for rainfall KE under BR09_S, BR09_C, BR03_S, and BR03_C, particularly the KE_{mm}–D_m relationship.

(3) For the entire dataset and three seasons, the mean Z_h was close to 21.6, 20.4, 22.7, and 20.9 dBZ, respectively. The mean Z_{dr} was largest (smallest) at 0.388 (0.269) dB in summer (spring), and the mean K_{dp} was largest (smallest) at 0.070 (0.029) $^\circ$ km^{-1} in summer (fall). Dual-polarization radar QPE algorithms differed seasonally. The coefficient $f(g)$ of the $R(Z_h)$ algorithm varied from 0.064 (0.491) to 0.072 (0.516), and the coefficient $h(i)$ of the $R(K_{dp})$ algorithm varied from 13.097 (0.649) to 14.655 (0.680) between different seasons. For the entire dataset and all seasons, the double-parameter algorithms were better than the single-parameter algorithms. Moreover, the $R(K_{dp}, Z_{dr})$ [$R(K_{dp})$] algorithm was superior to the $R(Z_h, Z_{dr})$ [$R(Z_h)$] algorithm.

(4) Differences were found in different seasons and types of rainfall under BR03 and BR09 for the four types of dual-polarization radar QPE algorithms. For different seasons and rainfall types in BR03 and BR09, the double-parameter algorithms were better than the single-parameter algorithms, and the $R(K_{dp})$ algorithm was superior to the

$R(Z_h)$ algorithm. For BR09_C, the $R(Z_h, Z_{dr})$ algorithm performed the best (worst) in spring (fall), while for BR09_S, the $R(K_{dp}, Z_{dr})$ algorithm performed the best (worst) in summer (spring). For BR03_C (BR03_S), the double-parameter algorithm exhibited the best performance in spring (summer).

The results of this study show that it is necessary to consider different rainfall types and seasons, as well as classification methods for rainfall types, when applying RKEE and dual-polarization radar QPE. In this process, choosing a suitable estimator ($KE_{time}(R)$, $KE_{mm}(D_m)$, $R(K_{dp})$, $R(Z_h)$, $R(K_{dp},Z_{dr})$, or $R(Z_h,Z_{dr})$) is key to improving the accuracy of estimating rainfall *KE* and *R*. However, it is necessary to establish a denser DSD observation network and to use various satellite observations to further obtain RKEE schemes and dual-polarization radar QPE algorithms over the Tianshan Mountains from a larger spatial scale.

Author Contributions: Conceptualization, Y.Z. and L.Y.; data curation, Y.Z. and X.L. (Xinyu Lu); formal analysis, Y.Z.; funding acquisition, Y.Z. and L.Y.; methodology, Y.Z., Z.T. and Y.J.; project administration, X.L. (Xiaomeng Li), Z.T. and Y.J.; resources, Y.Z. and L.Y.; supervision, A.A., Y.Z. and L.Y.; writing—original draft, Y.Z.; writing—review and editing, Y.Z. All authors have read and agreed to the published version of the manuscript.

Funding: This research was funded by Natural Science Foundation of Xinjiang Uygur Autonomous Region (Grant No. 2022D01B227), National Natural Science Foundation of China (Grant No. 42305080), Tianshan Mountains Talent Project (Grant No. 2022TSYCLJ0003), Key Research and Development Program of Xinjiang Uygur Autonomous Region (Grant No. 2023B03019-1), and S&T Development Fund of IDM (Grant No. KJFZ202401).

Data Availability Statement: The raw data supporting the conclusions of this article will be made available by the authors on request.

Acknowledgments: The authors would like to thank the Institute of Desert Meteorology, China Meteorological Administration, Urumqi, for providing the data of disdrometer. Thanks also goes to the reviewers for their thorough comments that really helped to improve the manuscript.

Conflicts of Interest: The authors declare no conflicts of interest.

References

1. Rosenfeld, D.; Ulbrich, C.W. Cloud microphysical properties, processes, and rainfall estimation opportunities. *Meteorol. Monogr.* **2003**, *30*, 237–258.
2. Zhang, G.; Sun, J.; Brandes, E.A. Improving parameterization of rain microphysics with disdrometer and radar observations. *J. Atmos. Sci.* **2006**, *63*, 1273–1290.
3. Mason, B.J. Physics of clouds and precipitation. *Nature* **1954**, *174*, 957–959.
4. Fornis, R.L.; Vermeulen, H.R.; Nieuwenhuis, J.D. Kinetic Energy–Rainfall Intensity Relationship for Central Cebu, Philippines for Soil Erosion Studies. *J. Hydrol.* **2005**, *300*, 20–32. [CrossRef]
5. Van, L.N.; Le, X.-H.; Nguyen, G.V.; Yeon, M.; May, D.T.T.; Lee, G. Comprehensive Relationships between Kinetic Energy and Rainfall Intensity Based on Precipitation Measurements from an OTT Parsivel2 Optical Disdrometer. *Front. Environ. Sci.* **2022**, *10*, 985516.
6. Lim, Y.S.; Kim, J.K.; Kim, J.W.; Park, B.I.; Kim, M.S. Analysis of the Relationship between the Kinetic Energy and Intensity of Rainfall in Daejeon, Korea. *Quat. Int.* **2015**, *384*, 107–117. [CrossRef]
7. Kinnell, P.I.A. Rainfall Intensity-Kinetic Energy Relationships for Soil Loss Prediction1. *Soil Sci. Soc. Am. J.* **1981**, *45*, 153.
8. Steiner, M.; Smith, J.A. Reflectivity, Rain Rate, and Kinetic Energy Flux Relationships Based on Raindrop Spectra. *J. Appl. Meteorol.* **2000**, *39*, 1923–1940. [CrossRef]
9. Seela, B.K.; Janapati, J.; Kalath Unnikrishnan, C.; Lin, P.-L.; Le Loh, J.; Chang, W.-Y.; Kumar, U.; Reddy, K.K.; Lee, D.-I.; Venkatrami Reddy, M. Raindrop Size Distributions of North Indian Ocean Tropical Cyclones Observed at the Coastal and Inland Stations in South India. *Remote Sens.* **2021**, *13*, 3178. [CrossRef]
10. Ryzhkov, A.V.; Zrnic, D.S. Comparison of dual polarization radar estimators of rain. *J. Atmos. Ocean. Technol.* **1995**, *12*, 249–256. [CrossRef]
11. Liao, L.; Meneghini, R.; Tokay, A. Uncertainties of GPM DPR rain estimates caused by DSD parameterizations. *J. Appl. Meteor. Climatol.* **2014**, *53*, 2524–2537. [CrossRef]
12. Chen, B.; Yang, J.; Pu, J. Statistical characteristics of raindrop size distribution in the Meiyu season observed in eastern China. *J. Meteorol. Soc. Jpn.* **2013**, *91*, 215–227. [CrossRef]

13. Zhang, Z.; Li, H.; Li, D.; Qi, Y. Spatial Variability of Raindrop Size Distribution at Beijing City Scale and Its Implications for Polarimetric Radar QPE. *Remote Sens.* **2023**, *15*, 3964. [CrossRef]
14. Chen, G.; Zhao, K.; Zhang, G.; Huang, H.; Liu, S.; Wen, L.; Yang, Z.; Yang, Z.; Xu, L.; Zhu, W. Improving Polarimetric C-Band Radar Rainfall Estimation with Two-Dimensional Video Disdrometer Observations in Eastern China. *J. Hydrometeorol.* **2017**, *18*, 1375–1391. [CrossRef]
15. Cao, Q.; Zhang, G.; Brandes, E.A.; Schuur, T.J. Polarimetric radar rain estimation through retrieval of drop size distribution using a Bayesian approach. *J. Appl. Meteorol. Climatol.* **2010**, *49*, 973–990. [CrossRef]
16. Ulbrich, C.W. Natural variations in the analytical form of the raindrop size distribution. *J. Clim. Appl. Meteorol.* **1983**, *22*, 1764–1775. [CrossRef]
17. Tokay, A.; Short, D.A. Evidence from tropical raindrop spectra of the origin of rain from stratiform versus convective clouds. *J. Appl. Meteorol.* **1996**, *35*, 355–371. [CrossRef]
18. Bringi, V.N.; Chandrasekar, V.; Hubbert, J.; Gorgucci, E.; Randeu, W.L.; Schoenhuber, M. Raindrop size distribution in different climatic regimes from disdrometer and dual-polarized radar analysis. *J. Atmos. Sci.* **2003**, *60*, 354–365. [CrossRef]
19. Konwar, M.; Das, S.K.; Deshpande, S.M.; Chakravarty, K.; Goswami, B.N. Microphysics of clouds and rain over the Western Ghat. *J. Geophys. Res. Atmos.* **2014**, *119*, 6140–6159. [CrossRef]
20. Chen, B.; Hu, Z.; Liu, L.; Zhang, G. Raindrop Size Distribution Measurements at 4500 m on the Tibetan Plateau during TIPEX-III. *J. Geophys. Res. Atmos.* **2017**, *12211*, 11092–12006.
21. Seela, B.K.; Janapati, J.; Lin, P.-L.; Reddy, K.K.; Shirooka, R.; Wang, P.K. A Comparison Study of Summer Season Raindrop Size Distribution between Palau and Taiwan, Two Islands in Western Pacific. *J. Geophys. Res. Atmos.* **2017**, *122*, 11–787. [CrossRef]
22. Suh, S.-H.; You, C.-H.; Lee, D.-I. Climatological characteristics of raindrop size distributions in Busan, Republic of Korea. *Hydrol. Earth Syst. Sci.* **2016**, *20*, 193–207. [CrossRef]
23. Wen, L.; Zhao, K.; Chen, G. Drop size distribution characteristics of seven typhoons in China. *J. Geophys. Res. Atmos.* **2018**, *123*, 6529–6548. [CrossRef]
24. Zheng, J.; Liu, L.; Chen, H. Characteristics of warm clouds and precipitation in South China during the pre-flood season using datasets from a cloud radar, a ceilometer, and a disdrometer. *Remote Sens.* **2019**, *11*, 3045. [CrossRef]
25. Zhang, A.; Hu, J.; Chen, S. Statistical characteristics of raindrop size distribution in the monsoon season observed in southern China. *Remote Sens.* **2019**, *11*, 432. [CrossRef]
26. Wen, L.; Zhao, K.; Zhang, G. Statistical characteristics of raindrop size distributions observed in East China during the Asian summer monsoon season using 2-D video disdrometer and Micro Rain Radar data. *J. Geophys. Res. Atmos.* **2016**, *121*, 2265–2282. [CrossRef]
27. Pu, K.; Liu, X.; Wu, Y.; Hu, S.; Liu, L.; Gao, T. A comparison study of raindrop size distribution among five sites at the urban scale during the East Asian rainy season. *J. Hydrol.* **2020**, *590*, 125500. [CrossRef]
28. Wen, L.; Zhao, K.; Wang, M. Seasonal variations of observed raindrop size distribution in East China. *Adv. Atmos. Sci.* **2019**, *36*, 346–362. [CrossRef]
29. Zhang, H.; Zhang, Y.; He, H. Comparison of raindrop size distributions in a midlatitude continental squall line during different stages as measured by Parsivel over East China. *J. Appl. Meteorol. Climatol.* **2017**, *56*, 2097–2111. [CrossRef]
30. Luo, L.; Guo, J.; Chen, H. Microphysical characteristics of rainfall observed by a 2DVD disdrometer during different seasons in Beijing, China. *Remote Sens.* **2021**, *13*, 2303. [CrossRef]
31. Ma, Y.; Ni, G.; Chandra, C.V. Statistical characteristics of raindrop size distribution during rainy seasons in the Beijing urban area and implications for radar rainfall estimation. *Hydrol. Earth Syst. Sci.* **2019**, *23*, 4153–4170. [CrossRef]
32. Ji, L.; Chen, H.N.; Li, L.; Chen, B.J.; Xiao, X.; Chen, M.; Zhang, G.F. Raindrop size distributions and rain characteristics observed by a PARSIVEL disdrometer in Beijing, Northern China. *Remote Sens.* **2019**, *11*, 1479. [CrossRef]
33. Wang, G.; Zhou, R.; Zhaxi, S.; Liu, S. Raindrop size distribution measurements on the Southeast Tibetan Plateau during the STEP project. *Atmos. Res.* **2021**, *249*, 105311. [CrossRef]
34. Wang, G.; Li, R.; Sun, J. Comparative analysis of the characteristics of rainy season raindrop size distributions in two typical regions of the Tibetan Plateau. *Adv. Atmos. Sci.* **2022**, *39*, 1062–1078. [CrossRef]
35. Janapati, J.; Seela, B.K.; Lin, P.L.; Lan, C.H.; Tu, C.C.; Kumar, U.; Huang, M.Q. An assessment of rainfall kinetic energy functional relationships with GPM DPR. *J. Hydrol.* **2023**, *617*, 128754. [CrossRef]
36. Wu, H.; Niu, S.; Zhou, Y.; Sun, J.; Lv, J.; He, Y. Characteristics of Raindrop Size Distributions in the Southwest Mountain Areas of China According to Seasonal Variation and Rain Types. *Remote Sens.* **2023**, *15*, 1246. [CrossRef]
37. Marshall, J.S.; Palmer, W.M. The distribution of raindrops with size. *J. Meteor.* **1948**, *5*, 165–166. [CrossRef]
38. Fulton, R.A.; Breidenbach, J.P.; Seo, D.-J. The WSR-88D Rainfall Algorithm. *Weather. Forecast.* **1998**, *13*, 377–395. [CrossRef]
39. Atlas, D.; Ulbrich, C.W.; Marks, F.D. Systematic variation of drop size and radar-rainfall relations. *J. Geophys. Res.* **1999**, *104*, 6155–6169. [CrossRef]
40. Ulbrich, C.W.; Atlas, D. Microphysics of raindrop size spectra: Tropical continental and maritime storms. *J. Appl. Meteor. Climatol.* **2007**, *46*, 1777–1791. [CrossRef]
41. Janapati, J.; Seela, B.K.; Lin, P.-L. Raindrop size distribution characteristics of Indian and Pacific Ocean tropical cyclones observed at India and Taiwan sites. *J. Meteor. Soc. Jpn.* **2020**, *98*, 299–317. [CrossRef]

42. Janapati, J.; Seela, B.K.; Lin, P.-L.; Lee, M.-T.; Joseph, E. Microphysical features of typhoon and non-typhoon rainfall observed in Taiwan, an island in the northwestern Pacific. *Hydrol. Earth Syst. Sci.* **2021**, *25*, 4025–4040. [CrossRef]
43. Kim, H.-J.; Jung, W.; Suh, S.-H.; Lee, D.-I.; You, C.-H. The Characteristics of raindrop size distribution at windward and leeward side over mountain area. *Remote Sens.* **2022**, *14*, 2419. [CrossRef]
44. Li, R.; Wang, G.; Zhou, R.; Zhang, J.; Liu, L. Seasonal variation in microphysical characteristics of precipitation at the entrance of water vapor channel in Yarlung Zangbo Grand Canyon. *Remote Sens.* **2022**, *14*, 3149. [CrossRef]
45. Cifelli, R.; Chandrasekar, V.; Lim, S.; Kennedy, P.C.; Wang, Y.; Rutledge, S.A. A new dual-polarization radar rainfall algorithm: Application in Colorado precipitation events. *J. Atmos. Ocean. Technol.* **2011**, *28*, 352–364. [CrossRef]
46. You, C.-H.; Kang, M.; Lee, D.-I. Rainfall estimation by S-band polarimetric radar in Korea. Part I: Preprocessing and preliminary results. *Meteorol. Appl.* **2014**, *21*, 975–983. [CrossRef]
47. Brandes, E.A.; Zhang, G.; Vivekanandan, J. Experiments in rainfall estimation with a polarimetric radar in a subtropical environment. *J. Appl. Meteorol.* **2002**, *41*, 674–685. [CrossRef]
48. Li, Q.; Wei, J.; Yin, J.; Qiao, Z.; Cao, J.; Shi, Y. Microphysical characteristics of raindrop size distribution and implications for radar rainfall estimation over the northeastern Tibetan Plateau. *J. Geophys. Res. Atmos.* **2022**, *127*, e2021JD035575. [CrossRef]
49. You, C.-H.; Suh, S.-H.; Jung, W.; Kim, H.-J.; Lee, D.-I. Dual-Polarization Radar-Based Quantitative Precipitation Estimation of Mountain Terrain Using Multi-Disdrometer Data. *Remote Sens.* **2022**, *14*, 2290. [CrossRef]
50. Zhang, J.B.; Deng, Z.F. *A Generality of Rainfall in Xinjiang*; Meteorological Press: Beijing, China, 1987; pp. 1–10. (In Chinese)
51. Yang, L.M.; Li, X.; Zhang, G.X. Some advances and problems in the study of heavy rain in Xinjiang. *Clim. Environ. Res.* **2011**, *16*, 188–198. (In Chinese)
52. Zeng, Y.; Yang, L. Triggering mechanism of an extreme rainstorm process near the Tianshan Mountains in Xinjiang, an arid region in China, based on a numerical simulation. *Adv. Meteorol.* **2020**, *2020*, 8828060. [CrossRef]
53. Zeng, Y.; Yang, L.; Zhang, Z.; Tong, Z.; Li, J.; Liu, F.; Zhang, J.; Jiang, Y. Characteristics of clouds and raindrop size distribution in Xinjiang, using cloud radar datasets and a disdrometer. *Atmosphere* **2020**, *11*, 1382. [CrossRef]
54. Zeng, Y.; Yang, L.; Tong, Z.; Jiang, Y.; Zhang, Z.; Zhang, J.; Zhou, Y.; Li, J.; Liu, F.; Liu, J. Statistical characteristics of raindrop size distribution during rainy seasons in Northwest China. *Adv. Meteorol.* **2021**, *2021*, 6667786. [CrossRef]
55. Zeng, Y.; Tong, Z.; Jiang, Y.; Zhou, Y. Microphysical characteristics of seasonal rainfall observed by a Parsivel disdrometer in the Tianshan Mountains, China. *Atmos. Res.* **2022**, *280*, 106459. [CrossRef]
56. Zeng, Y.; Yang, L.; Tong, Z.; Jiang, Y.; Chen, P.; Zhou, Y. Characteristics and applications of summer season raindrop size distributions based on a PARSIVEL^2 disdrometer in the western Tianshan Mountains (China). *Remote Sens.* **2022**, *14*, 3988. [CrossRef]
57. Zeng, Y.; Yang, L.; Zhou, Y.; Tong, Z.; Jiang, Y.; Chen, P. Characteristics of orographic raindrop size distribution in the Tianshan Mountains, China. *Atmos. Res.* **2022**, *278*, 106332. [CrossRef]
58. Zeng, Y.; Yang, L.; Zhou, Y.; Tong, Z.; Jiang, Y. Statistical characteristics of summer season raindrop size distribution in the western and central Tianshan Mountains in China. *J. Meteor. Soc. Jpn.* **2022**, *100*, 855–872. [CrossRef]
59. Zeng, Y.; Yang, L.; Li, J.; Jiang, Y.; Tong, Z.; Li, X.; Li, H.; Liu, J.; Lu, X.; Zhou, Y. Seasonal variation of microphysical characteristics for different rainfall types in the Tianshan Mountains of China. *Atmos. Res.* **2023**, *295*, 107024. [CrossRef]
60. Zeng, Y.; Li, J.; Yang, L.; Li, H.; Li, X.; Tong, Z.; Jiang, Y.; Liu, J.; Zhang, J.; Zhou, Y. Microphysical Characteristics of Raindrop Size Distribution and Implications for Dual-Polarization Radar Quantitative Precipitation Estimations in the Tianshan Mountains, China. *Remote Sens.* **2023**, *15*, 2668. [CrossRef]
61. Chen, P.; Wang, P.; Li, Z.; Yang, Y.; Jia, Y.; Yang, M.; Peng, J.; Li, H. Raindrop Size Distribution Characteristics of Heavy Precipitation Events Based on a PWS100 Disdrometer in the Alpine Mountains, Eastern Tianshan, China. *Remote Sens.* **2023**, *15*, 5068. [CrossRef]
62. Bringi, V.N.; Williams, C.R.; Thurai, M. Using dual-polarized radar and dual-frequency profiler for DSD characterization: A case study from Darwin, Australia. *J. Atmos. Oceanic Technol.* **2009**, *26*, 2107–2122. [CrossRef]
63. Löffler-Mang, M.; Joss, J. An optical disdrometer for measuring size and velocity of hydrometeors. *J. Atmos. Ocean. Technol.* **2000**, *17*, 130–139. [CrossRef]
64. Yuter, S.E.; Kingsmill, D.E.; Nance, L.B.; Löffler-Mang, M. Observations of precipitation size and fall speed characteristics within coexisting rain and wet snow. *J. Appl. Meteorol.* **2006**, *45*, 1450–1464. [CrossRef]
65. Huang, C.; Chen, S.; Zhang, A.; Pang, Y. Statistical characteristics of raindrop size distribution in monsoon season over South China Sea. *Remote Sens.* **2021**, *13*, 2878. [CrossRef]
66. Chen, B.; Yang, J.; Gao, R.; Zhu, K.; Zou, C.; Gong, Y.; Zhang, R. Vertical variability of the raindrop size distribution in typhoons observed at the Shenzhen 356-m meteorological tower. *J. Atmos. Sci.* **2020**, *77*, 4171–4187. [CrossRef]
67. Fu, Z.; Dong, X.; Zhou, L.; Cui, W.; Wang, J.; Wan, R.; Leng, L.; Xi, B. Statistical characteristics of raindrop size distributions and parameters in Central China during the Meiyu seasons. *J. Geophys. Res. Atmos.* **2020**, *125*, e2019JD031954. [CrossRef]
68. Liu, X.; Xue, L.; Chen, B.; Zhang, Y. Characteristics of raindrop size distributions in Chongqing observed by a dense network of disdrometers. *J. Geophys. Res. Atmos.* **2021**, *126*, e2021JD035172. [CrossRef]
69. Sreekanth, T.S.; Varikoden, H.; Sukumar, N.; Mohan Kumar, G. Microphysical characteristics of rainfall during different seasons over a coastal tropical station using disdrometer. *Hydrol. Process.* **2017**, *31*, 2556–2565. [CrossRef]

70. Tokay, A.; Petersen, W.A.; Gatlin, P.; Wingo, M. Comparison of raindrop size distribution measurements by collocated disdrometers. *J. Atmos. Ocean. Technol.* **2013**, *30*, 1672–1690. [CrossRef]
71. Friedrich, K.; Higgins, S.; Masters, F.J.; Lopez, C.R. Articulating and stationary PARSIVEL disdrometer measurements in conditions with strong Winds and heavy rainfall. *J. Atmos. Oceanic Technol.* **2013**, *30*, 2063–2080. [CrossRef]
72. Salles, C.; Poesen, J.; Sempere-Torres, D. Kinetic energy of rain and its functional relationship with intensity. *J. Hydrol.* **2002**, *257*, 256–270. [CrossRef]
73. Van Dijk, A.; Bruijnzeel, L.A.; Rosewell, C.J. Rainfall intensity–kinetic energy relationships: A critical literature appraisal. *J. Hydrol.* **2002**, *261*, 1–23. [CrossRef]
74. Tokay, A.; Wolff, D.B.; Petersen, W.A. Evaluation of the new version of the laser-optical disdrometer, OTT Parsivel^2. *J. Atmos. Ocean. Technol.* **2014**, *31*, 1276–1288. [CrossRef]
75. Battaglia, A.; Rustemeier, E.; Tokay, A. PARSIVEL snow observations: A critical assessment. *J. Atmos. Oceanic Technol.* **2010**, *27*, 333–344. [CrossRef]
76. Testud, J.; Oury, S.; Amayenc, P.; Black, R.A. The concept of "normalized" distributions to describe raindrop spectra: A tool for cloud physics and cloud remote sensing. *J. Appl. Meteorol.* **2001**, *40*, 1118–1140. [CrossRef]
77. Kalogiros, J.; Anagnostou, M.N.; Anagnostou, E.N. Optimum estimation of rain microphysical parameters from X-band dual-polarization radar observables. *IEEE Trans. Geosci. Remote Sens.* **2013**, *51*, 3063–3076. [CrossRef]
78. Leinonen, J. High-level interface to T-matrix scattering calculations: Architecture, capabilities and limitations. *Opt. Express* **2014**, *22*, 1655–1660. [CrossRef]
79. Waterman, P.C. Matrix formulation of electromagnetic scattering. *Proc. IEEE* **1965**, *53*, 805–812. [CrossRef]
80. Tokay, A.; Short, D.A.; Williams, C.R.; Ecklund, W.L.; Gage, K.S. Tropical Rainfall Associated with Convective and Stratiform Clouds: Intercomparison of Disdrometer and Profiler Measurements. *J. Appl. Meteorol.* **1999**, *38*, 302–320. [CrossRef]
81. Dolan, B.; Fuchs, B.; Rutledge, S.A.; Barnes, E.A.; Thompson, E.J. Primary modes of global drop size distributions. *J. Atmos. Sci.* **2018**, *75*, 1453–1476. [CrossRef]
82. Lee, M.T.; Lin, P.L.; Chang, W.Y.; Seela, B.K.; Janapati, J. Microphysical characteristics and types of precipitation for different seasons over North Taiwan. *J. Meteor. Soc. Jpn.* **2019**, *97*, 841–865. [CrossRef]
83. Seela, B.K.; Janapati, J.; Lin, P.-L.; Lan, C.-H.; Shirooka, R.; Hashiguchi, H.; Reddy, K.K. Raindrop Size Distribution Characteristics of the Western Pacific Tropical Cyclones Measured in the Palau Islands. *Remote Sens.* **2022**, *14*, 470. [CrossRef]
84. Guo, Z.; Hu, S.; Liu, X.; Chen, X.; Zhang, H.; Qi, T.; Zeng, G. Improving S-band polarimetric radar monsoon rainfall estimation with two-dimensional video disdrometer observations in South China. *Atmosphere* **2021**, *12*, 831. [CrossRef]

Disclaimer/Publisher's Note: The statements, opinions and data contained in all publications are solely those of the individual author(s) and contributor(s) and not of MDPI and/or the editor(s). MDPI and/or the editor(s) disclaim responsibility for any injury to people or property resulting from any ideas, methods, instructions or products referred to in the content.